Earth and Space Science

RESEARCH ARTICLE
10.1029/2020EA001086

Special Section:
InSight at Mars

Calibration of the HP^3 Radiometer on InSight

N. T. Mueller[1], J. Knollenberg[1], M. Grott[1], E. Kopp[2], I. Walter[2], C. Krause[3], T. Hudson[4], T. Spohn[1,5], and S. Smrekar[4]

[1]Institute of Planetary Research, German Aerospace Center (DLR), Berlin, Germany, [2]Institute of Optical Sensor Systems, German Aerospace Center (DLR), Berlin, Germany, [3]Microgravity User Support Center, German Aerospace Center (DLR), Cologne, Germany, [4]Jet Propulsion Laboratory, California Institute of Technology, Pasadena, CA, USA, [5]International Space Science Institute (ISSI), Bern, Switzerland

Abstract The Heatflow and Physical Properties Package (HP^3) radiometer is currently operating on Mars, observing two spots approximately 1 and 3 m north-north-west of the InSight lander. The instrument has primary sensors that are sensitive in the range of 8 to 14 μm and two more sensors with more narrow spectral ranges per field of view. The radiometer underwent radiometric and geometric calibration at DLR—Berlin; and on Mars radiometric self-calibration is performed regularly. The self-calibration confirms that one of the two primary sensors has been stable since the ground calibration, but environmental parameters that are likely associated with the thermal contact of sensor and instrument main body may have slightly changed. The other primary sensor has increased in sensitivity for an unknown reason but is still within expectation from the sensor design. The uncertainty of the two primary sensors is approximately 3 K at night, with somewhat larger errors in the late afternoon. This estimate includes the effect of sensitivity changes that would be too small to be reliably detected by the self-calibration.

Key Points:
- We describe the calibration of the HP^3 radiometer measuring surface brightness temperature on Mars next to the Insight lander
- Regular self-calibration measurements on Mars ensure an uncertainty of 3 K at night

Correspondence to:
N. T. Mueller,
nils.mueller@dlr.de

Citation:
Mueller, N. T., Knollenberg, J., Grott, M., Kopp, E., Walter, I., Krause, C., et al. (2020). Calibration of the HP^3 radiometer on InSight. *Earth and Space Science*, *7*, e2020EA001086. https://doi.org/10.1029/2020EA001086

Received 13 JAN 2020
Accepted 11 MAR 2020
Accepted article online 18 MAR 2020

1. Introduction

The Mars lander InSight (Banerdt et al., 2020) carries the Heatflow and Physical Properties Package (HP^3 Spohn et al., 2018). The instrument is designed to deploy an instrumented probe and tether into the subsurface of Mars to measure the thermal gradient and thermal conductivity of the regolith in order to derive the heat flow from the interior. The planetary heat flow is an important parameter for the understanding of the planets thermal evolution (e.g., Plesa, Grott, Tosi, et al., 2016; Plesa et al., 2015, 2018; Smrekar et al., 2019).

External forcing of the surface temperature results in a perturbation of this heat flow (Grott et al., 2007; Grott, 2009; Morgan et al., 2017; Plesa, Grott, Lemmon, et al., 2016; Siegler et al., 2017), which, however, decays quickly with depth depending on the periodicity of the forcing and thermal conductivity of the soil. The seasonal and diurnal perturbations are expected to be negligible if the HP^3 heat flow probe can be deployed to the full length of the tether of 5 m and if it is possible to average temperature over a whole seasonal cycle.

In case the full depth cannot be reached or if measurements cannot take place over a full Mars year, the HP^3 instrument also includes a radiometer (Kopp et al., 2016), abbreviated to RAD, to observe the surface brightness temperature and thus the external forcing directly. In situ radiometers can also be used to derive thermophysical properties of the observed ground, such as thermal inertia (e.g., Fergason et al., 2006; Golombek et al., 2020; Grott et al., 2019; Vasavada et al., 2017). The InSight lander also has a comprehensive suite of meteorological sensors, which enable atmospheric science that is enhanced by the RAD data (Banfield et al., 2020; Spiga et al., 2018).

The HP^3-RAD radiometer is based on the designs of the MASCOT Radiometer (Grott et al., 2017) on Hayabusa 2, of the MERTIS instrument on Bepi-Colombo (Hiesinger & Helbert, 2010; Walter et al., 2006), and of the MUPUS Thermal Mapper on Rosetta (Spohn et al., 2007, 2015). The HP^3-RAD was radiometrically calibrated in a space simulation chamber under conditions simulating the Mars environment over 2 weeks in April 2017. Onboard calibration occurred regularly after landing starting in December 2018.

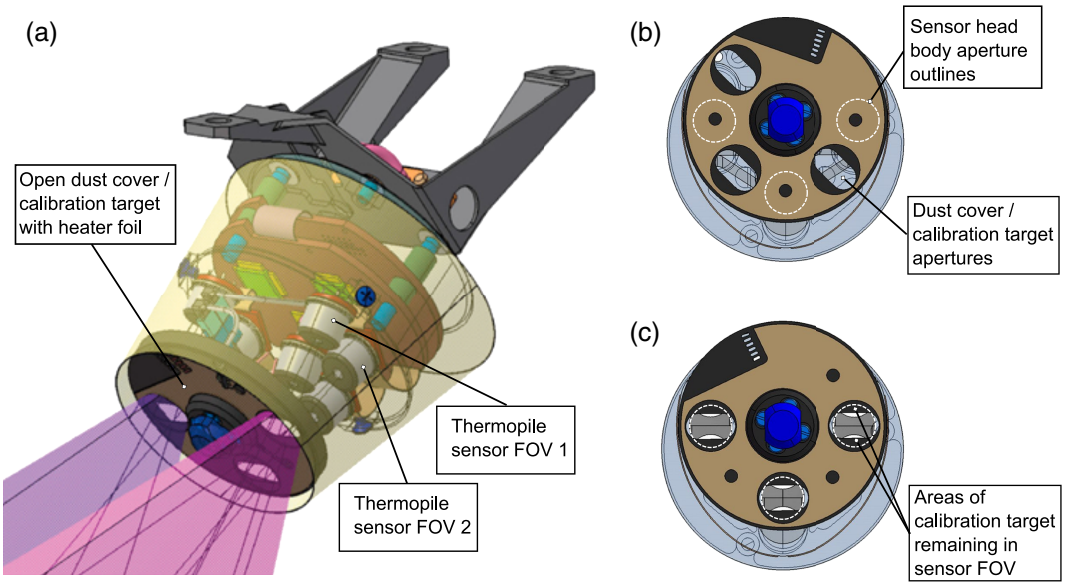

Figure 1. Sketch showing details of the mechanical design relevant for calibration. (a) Perspective, semitransparent view. (b) View along the normal of the closed dust cover/calibration target. (c) Same view with the cover in the open state.

2. Radiometer Description

2.1. Overview

Figure 1a shows an semitransparent representation of the radiometer sensor head (SH). The SH is mounted underneath the InSight lander deck with the apertures normal looking 40° down relative to the deck. The sensors are protected by a dust cover that was closed during landing and initial calibration (Figure 1b). To open the cover it was rotated by a one-time mechanism to the open position (Figure 1c). The dust cover is equipped with a heater and a temperature sensor and is used as a calibration target (CT). The apertures in the dust cover are smaller than field of view (FOV) of the sensors so that after opening some further calibration can take place, similar to the concept of the Rover Environmental Monitoring Station (Gómez-Elvira et al., 2012), Ground Temperature Sensor (GTS Sebastián et al., 2010b) instrument on the Mars Science Laboratory rover, and the Thermal Infrared Sensor (TIRS Pérez-Izquierdo et al., 2018) on the Mars 2020 rover.

The six thermopile sensors are housed in a temperature controlled body (not shown), with a pair of sensors sharing each aperture. The two sensors of each aperture have different orientations, observing at a relative elevation of −15° and +15° relative to the aperture normal. As a result the two sensors observe two spots in different distances from the lander, approximately 1 and 3 m. The closer spot is observed by FOV 1 and the farther spot is observed by FOV 2.

2.2. Sensors

The main sensing elements are TS-72 thermopile sensors from the Institute of Photonic Technology in Jena, Germany. These consist of a membrane with an absorber layer that is in radiative exchange with the observed surface via a band-pass filter window. The radiative exchange can be described by the net heat flux, that is, the difference of the incoming radiation flux absorbed by the absorber layer and the outgoing flux emitted by the absorber layer. The net radiative heat flux results in a minuscule temperature difference of the absorber layer relative to the rest of the sensor, which generates a voltage over a set of 72 Sb-Bi thermocouples on the membrane. The sensor packages also include a Platinum Thermometer with 100 Ω nominal resistance (PT100) to provide a more accurate estimate of the outgoing thermal emission flux. The sensors are filled with an inert gas, which protects the absorber layer but also increases heat transfer within the sensors and thus reduces the observable signal. The selection of the gas is a trade-off between low thermal conductivity and a condensation point that is above the lowest temperatures encountered during all mission phases, with krypton being the resulting choice.

The filter windows are three different band passes: a broad band pass from 8 to 14 μm, a more narrow, shorter-wavelength band pass from 8 to 10 μm, and a longer wavelength band pass from 15 to 19 μm. A plot of

the filter transmittances is shown in the HP^3 general description (Spohn et al., 2018). The 8 to 14 μm and the 15 to 19 μm band passes are the same as in the Rover Environmental Monitoring Station-GTS instrument, and the 8- to 10-μm band passes encompasses a region where Martian soils show high emissivity with little variability (Morgan et al., 2018; Ruff et al., 2006).

The six sensors are labeled according to FOV and SH aperture, that is, thermopile of FOV 1, Aperture 1 is TP11. TP12 and TP23 use the broad band pass from 8 to 14 μm, TP11 and TP22 use the band pass from 8–10 μm, and TP 13 and TP 21 use the 15- to 19-μm band pass. This configuration is in case that there is a failure in the CT temperature sensor. Then it is advantageous to observed the same aperture with two different spectral bands, because in theory this provides a chance to disentangle the surface temperature signal from that of the then unknown CT signal.

2.3. Electronics

The measured electric voltages of thermopile and temperature sensors are digitized in the SH electronics using two 24-bit analog to digital converters (ADCs) with eight differential channels. The measurements per ADC are three thermopile sensors with the three associated PT100s, one reference resistor with $R_{\mathrm{ref}} = 100\Omega$, and one additional PT100 for temperature control.

The raw thermopile voltage digital numbers D_{TC}, indicated by channels ending in "TC" in the raw data description, are translated to physical voltages by multiplication with a constant depending on the ADC and its configuration, here generally per digital number increment:

$$U_{\mathrm{TC}} = D_{\mathrm{TC}} 7.238926\mathrm{nV} \tag{1}$$

The PT100 raw data D_{PT}, indicated by channels including a "PT" in the raw data description, are accompanied by offset measurements O_{PT} where the ADC measures the voltage over the sensor without a source current. Additionally, each ADC measures the voltage over a stable reference resistor with $R_{\mathrm{ref}} = 100\,\Omega$, raw digital number D_{rref}, which is also accompanied by an offset measurement O_{rref}. The physical resistance values are calculated as follows:

$$R_{\mathrm{PT}} = \frac{D_{\mathrm{PT}} - O_{\mathrm{PT}}}{D_{\mathrm{rref}} - O_{\mathrm{rref}}} R_{\mathrm{ref}} \tag{2}$$

The temperature measurement of each sensor has to be calculated with the reference resistor connected to the same ADC, which is indicated by the numeral in the raw data channel name. The SH temperature is measured by ADC 1 and the CT temperature is measured by ADC 2. The resistances are then used to determine temperatures based on the standard calibration curve of platinum resistance thermometers (Preston-Thomas, 1990). Measured within the instrument are the sensor reference temperature T_{ref}, the SH temperature T_{SH}, used to stabilize the temperature of the sensors, and the CT temperature T_{CT}, which is also actively stabilized by a heater.

The PT100 sensors in the thermopile sensor packages providing T_{ref} are relevant to the radiometric calibration. These are thin film platinum resistance thermometers of the same type as those used in the HP^3 instrumented tether. During the calibration of the tether sensors only small deviations from the standard calibration curves were found (Grott et al., 2019). The instrument is operated and radiometrically calibrated at only three instrument temperature set points, deviations from the standard calibration curves would only introduce constant offsets to the thermopile voltage. These constant thermopile voltage offsets are determined during the radiometric calibration and subtracted, so that the use of standard calibration curves on the overall calibration is small.

2.4. Heaters

The instrument SH and the CT are temperature stabilized by a controlled current source operated by the back-end electronics (BEE) of HP^3. We found that the heater power required to keep the SH at a constant temperature is the best parameter available to correct the instrument for the impact of its thermal environment. The heater power value has to be reconstructed from the commanded parameter D_{PSH} of the current source, as well as BEE temperature T_{BEE} and BEE supply voltage U_{bus}. We use a function empirically derived during thermal vacuum tests of the BEE to describe the output of the current source:

$$I_{\mathrm{PSH}} = \left[\sum_{i=0}^{2} \sum_{j=0}^{2} k_{i,j} D_{\mathrm{PSH}}^{i} T_{\mathrm{BEE}}^{j} \right] (-0.88645 + 0.0673845\ \mathrm{V}^{-1}\ U_{\mathrm{bus}}) \tag{3}$$

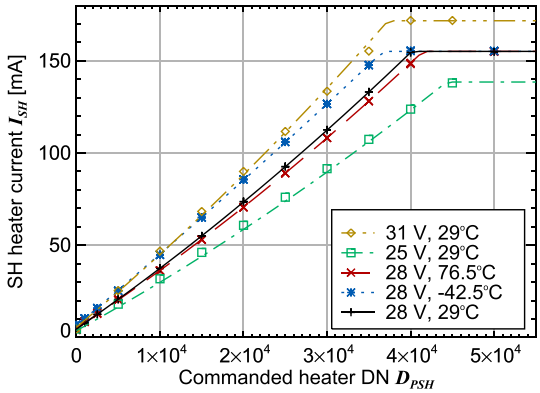

Figure 2. Measured data of heater current provided by the RAD sensor head current source over the range of tested BEE temperatures and supply voltages with empirical fits from equation (3).

where $k_{i,j}$ is a matrix of experimentally determined coefficients with unit $[k_{i,j}] = \mathrm{mA°C}^{-j}$ and i and j indicating columns and rows from top left, respectively:

$$k_{i,j} = \begin{bmatrix} 4.95423221588 & -2.12871748954 \times 10^{-2} & 2.92740616714 \times 10^{-4} \\ 3.34959849715 \times 10^{-3} & -8.83220491232 \times 10^{-6} & 5.09164159723 \times 10^{-8} \\ 1.29039134932 \times 10^{-8} & 1.11354592213 \times 10^{-10} & -1.00609538061 \times 10^{-12} \end{bmatrix} \tag{4}$$

The current source is limited by the supply voltage of the instrument to a maximum current:

$$I_{\max} = \frac{U_{\mathrm{bus}}}{(R_{\mathrm{SH}} + R_{\mathrm{BEE}})}, \tag{5}$$

where $R_{\mathrm{SH}} = 172\,\Omega$ is the SH heater resistance and $R_{\mathrm{BEE}} = 8.5\,\Omega$ is line resistance. The heater power that is dissipated in the SH is

$$P_{\mathrm{SH}} = R_{\mathrm{SH}} I_{\mathrm{PSH}}^2 \tag{6}$$

where I_{PSH} is subsituted by $I_{\max}$ in case the latter is smaller. Figure 2 shows the acquired data and the fitted function.

The largest fit residuals of observed data with equation (3) is $\Delta I_{\mathrm{PSH}} = 5$ mA. The corresponding error in heater power is

$$\Delta P_{\mathrm{SH}} = \frac{1}{2}\sqrt{R_{\mathrm{SH}} P_{\mathrm{SH}}}\,\Delta I_{\mathrm{PSH}}. \tag{7}$$

During tests with the nominal supply voltage of 28 V the fit residual is < 1 mA. This supply voltage was used during the radiometric calibration tests, so that the heater power errors in these tests are relatively small.

3. Radiometric Calibration

3.1. Mathematical Model

Under ideal circumstances is the signal by the thermopiles U_{TC} proportional to the net heat flux F at the sensor:

$$U_{\mathrm{TC}} = SF, \tag{8}$$

where S is the sensor sensitivity with the unit $[S] = \mathrm{V/W}$. This sensitivity involves the temperature difference that is maintained over the thermocouple junction pairs and therefore depends on the thermal conductivity of the fill-gas within the sensor package, which itself is a function of the gas temperature. The net radiative heat flux F is determined by the heat flux emitted by the environment and absorbed by the sensor with absorber area A minus the heat flux emitted by the absorber. This is calculated by integrating over the respective black-body functions B_λ and solid angle of the hemisphere in view of the absorber area:

$$F = A \int_0^{2\pi} \int_0^{\pi/2} \int_0^{\infty} \tau(\lambda,\vartheta)\varepsilon_{\mathrm{ref}}(\lambda)\left[\varepsilon(\lambda,\vartheta,\phi)B_\lambda(T(\vartheta,\phi)) - B_\lambda(T_{\mathrm{ref}})\right]\cos\vartheta \mathrm{d}\phi \sin\vartheta \mathrm{d}\vartheta \mathrm{d}\lambda, \tag{9}$$

where λ is wavelength, ϑ inclination relative to the absorber surface normal (i.e., the sensor boresight), ϕ is azimuth, $\varepsilon_{\mathrm{ref}}$ and T_{ref} are the sensor absorptivity and temperature, τ is the sensor window transmittance, and ε and T are the emissivity and temperature of the hemisphere in view of the absorber surface. This equation neglects any radiation reflected from the observed surface. It is possible to include this in the net flux (e.g., Hamm et al., 2018) but the reflectance of the observed ground in the spectral bands of the HP^3 RAD is expected to be small because the emissivity is close to unity (Morgan et al., 2018).

The thermopiles are housed in a sensor package thermally coupled to the temperature controlled radiometer body so that the inside of the package, including the absorber surface, is approximately isothermal. The inside of the package is coated with high emissivity paint and, with the small aperture seen from the absorber within the off-boresight angle $\vartheta < \vartheta_a = 10°$, resembles a cavity blackbody. Mathematically, we represent this by assuming in equation (9) that outside the cone defined by the aperture, $\vartheta > \vartheta_a$, it is $\tau(\vartheta) = 1$, $\varepsilon(\vartheta) = 1$, and $T(\vartheta) = T_{\mathrm{ref}}$. Further assuming that these variables within the cone defined by the aperture are uniform with respect to the viewing angle, the equation for the net heat flux reduces to

$$F = A\sin^2\vartheta_a\pi \int_0^\infty \tau(\lambda)\varepsilon_{\mathrm{ref}}(\lambda)\left[\varepsilon(\lambda)B_\lambda(T) - B_\lambda(T_{\mathrm{ref}})\right]\mathrm{d}\lambda. \tag{10}$$

The approximation of $T = T_{\mathrm{ref}}$ for $\vartheta > \vartheta_a$ is not perfect, in reality there are inhomogeneities. The temperature control stabilizes the temperature of the SH T_{SH} and the thermometers at the base plate of each thermopile deviate from this by a fraction of a K. The deviation is a near linear function of the heater power P_{SH} required to keep the SH temperature constant; however, this information is not sufficient to predict the total temperature inhomogeneity in view of the thermopile absorbers. For the GTS and Thermal Infrared Sensor radiometers on the Mars Science Laboratory and Mars 2020 rovers, the temperature inhomogeneity and the resulting heat exchange with the thermopile absorber have been parameterized in the form of a mathematical thermal model based on the geometry of the instrument and coefficients derived from tests (Pérez-Izquierdo et al., 2018; Sebastián et al., 2010a, 2010b). These radiometers are not actively temperature controlled and therefore have to operate under a wide range of temperatures and temperature change rates (Sebastián et al., 2011).

For the MARA radiometer (Grott et al., 2017) and the HP^3 radiometer, which are stabilized at defined temperatures by heaters distributed in the body housing the sensors, we use a simpler approach based on the power P_{SH} needed to keep the instrument SH at a constant temperature. In calibration tests observing a cavity blackbody at the same temperature as the SH (i.e., $T = T_{\mathrm{SH}}$, $T \approx T_{\mathrm{ref}}$ and $F \approx 0$ W) we observe an offset in measured U_{TC} that can be fitted well with a linear function of P_{SH}. This can be attributed to a residual radiative heat flux between absorber and sensor cap or temperature gradients resulting in temperature differences between the thermocouple junctions or a combination of both.

This offset, that is, the thermopile voltage recorded when the net radiative heat flux F is 0, needs to be accounted for when inverting the recorded voltages to brightness temperature. The equation that is fitted to the calibration data is therefore

$$U_{\mathrm{TC}} = C + H\,P_{\mathrm{SH}} + S\,F, \tag{11}$$

where offset voltage C, heater power response H, and sensitivity S are the calibration coefficients that have to be determined. Grott et al. (2017) fitted the MARA calibration data with an additional term proportional to F^2; however, we found that this does not significantly improve the residuals of the fit of HP^3 RAD data.

The CT in its open state further restricts the view of the outside with an aperture that is not axisymmetric around the boresight. In normal measurements the CT is controlled to be at the same temperature as the SH and therefore contributes little to the observed signal. In the self-calibration measurement, the CT temperature is varied relative to the SH temperature to provide the stimulus to derive the calibration coefficients. For the sake of simplicity we do not include these geometric details in the integral over the solid angle and instead use different calibration coefficients while keeping the same assumptions for the solid angle contributing to the signal. The details of the different varieties of the calibration coefficients are described in the following in the sections dealing with their experimental determination.

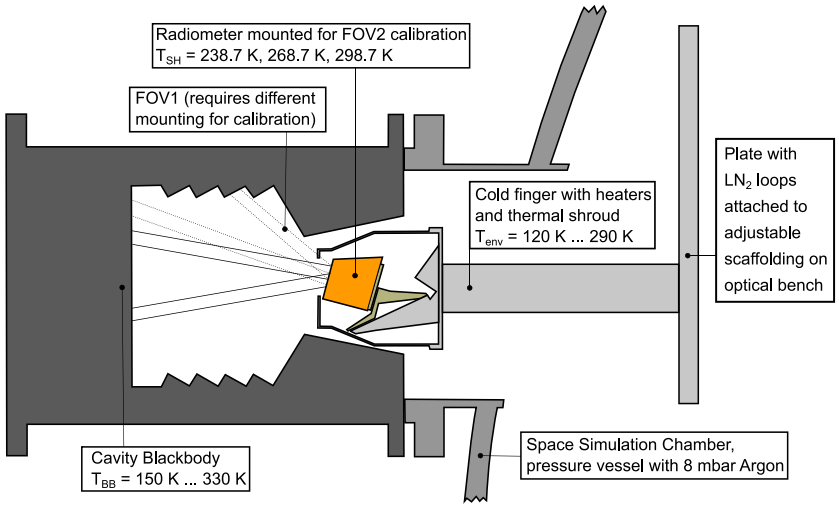

Figure 3. Sketch showing the setup of the ground calibration tests based on the BB100 cavity blackbody (Sapritsky et al., 2003). Shown is only the mounting position for FOV 2, observing the spot farther from the lander.

3.2. Calibration Data Acquisition
3.2.1. On Earth

The calibration setup, see Figure 3, had two independent temperature controlled components, the cavity black-body simulating the observed surface with temperature T_{BB} and a thermal shroud, simulating the thermal environment of the instrument with temperature T_{env}. The RAD was mounted in the shroud looking at the aperture of the cavity blackbody and is thermally stabilized by its own heaters. The two different FOVs of the RAD could not simultaneously observe the blackbody cavity because of the large angle between them. Therefore, the instrument had to be mounted in two different positions so that each of the two FOVs observed the blackbody cavity, and the calibration procedure had to be repeated for each FOV.

The simulation chamber was filled with 8 mbar of Argon to simulate the Mars atmosphere. CO_2, the main constituent of the Martian atmosphere, would freeze out at the liquid nitrogen loops that provide cooling to the blackbody and the thermal shroud and therefore had to be substituted by Argon, which has a lower freezing point but a similar molecular weight and thus similar thermal conductivity. The cavity blackbody provided the calibration standard for observed brightness temperatures of $T_{BB} = 150$ to 310 K with a thermal stability of 50 mK and an emissivity > 0.999 (Sapritsky et al., 2003). The thermal shroud provided a Mars-like thermal environment of $T_{env} = 170$ to 270 K.

The instrument is calibrated at three different set points of the SH temperature T_{SH} that are intended for different local true solar times (LTST) and seasons on Mars. The lowest-temperature set point of T_{SH} =238.7 K is intended for "night" measurements, approximately between 19 hr LTST and 10 hr LTST, while the other two set points of T_{SH} =268.7 K and T_{SH} =298.7 K are intended for measurements during the day, and to be chosen depending on the actual thermal environment at the landing site. Lower instrument temperatures are advantageous for measurement uncertainty and power consumption, but the choice is limited by electronics operating temperature range and the need to heat against the environment for stabilization.

The calibration procedure for each of the three set points consists of stabilizing the instrument for at least one hour in a thermal environment significantly below the instrument set point and then stabilizing the blackbody at eight to nine different temperatures for 20 min each. The resulting difference between T_{ref} and $T = T_{BB}$ provides variation of the net radiative heat flux F in equation (11) and thus constrains the sensitivity S coefficient. This is followed by stabilizing the blackbody at the instrument temperature set point to provide nominally zero net radiative heat flow F, while the environmental temperature is stabilized at four or five different temperatures for 1 hr each, which results in a variation of the heater power P_{SH} and thus constrains the heater response coefficient H in equation (11). The offset voltage at zero radiative heat

Table 1
Self-Calibration Sequences for the Three Different Instrument Temperature Set Points Presented as the Difference Between CT and SH Temperature $T_{CT} - T_{SH}$ in K

T_{SH} = 238.7 K			
Earth	Mars	T_{SH} = 268.7 K	T_{SH} = 298.7 K
0	0	0	0
18	5	−2	−3
5	9	15	10
0	18	0	0
−5	23	5	5
0	N/A	0	0

flow and heater power C is derived from the fit of equation (11) to the calibration data, since the instrument cannot be thermally stabilized at zero heater power.

The self-calibration was performed in the same setup, both with the CT open as well as with the CT closed. This consists of setting the blackbody and environment to a constant temperature and running the self-calibration mode of the instrument. The calibration sequence, provided in Table 1, starts and ends with the CT temperature (T_{CT}) being the same as that of the SH (T_{SH}) to provide nominally zero net radiative heat exchange (F). In between T_{CT} was varied relative to T_{SH} to constrain the sensitivity coefficient S. The sequence was repeated at several environmental temperatures to constrain the heater response H.

3.2.2. On Mars

After landing on Mars, RAD initially acquired data with the dust cover closed and $T_{CT} = T_{SH}$ to observe the effect of the thermal environment on the instrument without any direct signal from the Martian surface. Data were gathered for 5 min at each full local solar time hour for approximately 6 nights at T_{SH} =238.7 K, and 4 days at T_{SH} =268.7 K and approximately 1 day at T_{SH} =298.7 K. Figure 4 shows the data gathered on Sol 13 where between 10 and 19 hr LTST the instrument was operated at T_{SH} =298.7 K, the highest and therefore noisiest set point. The observation noise is estimated from the standard deviation of the 23 data points gathered during 5 min of each hour. The noise is generally higher during times when the atmosphere is more turbulent but lower than 1.3 μV in any case. Electronic noise from readings of the reference resistor are typically on the order of 100 nV. The CT and sensor temperature stability is better than 100 mK in the worst case, which at the sensitivity of the sensors (section 3.3.2) translates (equations (8) and (10)) to a voltage of 900 nV. Temperature fluctuations that are not measured by any sensor, for example, in the thermopile housing, can probably account for the rest of the observed noise.

The self-calibration was run once for each instrument set point at an appropriate time of day to use heater power similar to that of science measurements. That means that the T_{SH} =238.7-K self-calibration was run at night, starting at approximately 2 a.m. LTST, while the other calibrations were started at noon. During the first self-calibration test, a design flaw was detected that was considered a possible risk of damage to the instrument under certain conditions. To avoid these conditions, the calibration procedure had to be changed for the night set point calibration to avoid any sequence where the CT temperature decreased relative to the preceding step (Table 1, second column). Another consequence of the risk described above was to move the day calibration to the late afternoon and is immediately followed by the night calibration so that the first measurement at T_{SH} =238.7 K occurs at 19:30 LTST.

On Sol 14, approximately 12 hr LTST the one-time mechanism of the dust cover was activated and it rotated so that its apertures aligned with the sensor FOVs. Approximately 25% of the FOV is still filled by the CT to enable further self-calibration runs, albeit with reduced accuracy due to the smaller calibration signal. These are typically performed for each set point once per 30 sols. After Sol 100 the sequence of the self-calibration runs was changed so that all three set points are on the same sol: T_{SH} = 298.7 K with the first measurement period at noon, T_{SH} = 268.7 K with the first measurement period at 16:54 LTST, and T_{SH} = 238.7 K directly following.

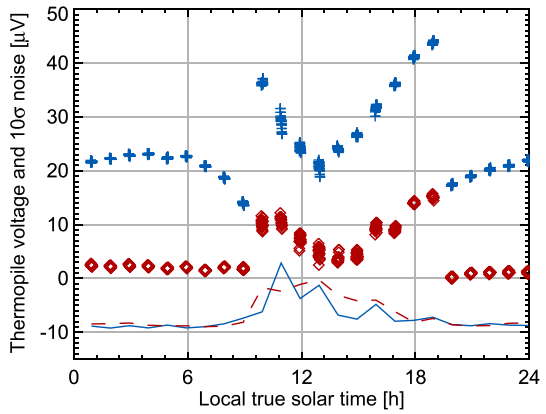

Figure 4. Thermopile voltage recorded on Sol 13 (symbols) with noise estimate (lines). The noise estimate is given as 10 standard deviations and offset by −10 μV for readability. Blue crosses and the solid line are from the FOV 1 broadband sensor, and the red diamonds and the dashed line are the FOV 2 broadband sensor. The CT is still closed on this sol.

3.3. Data Evaluation

The main objective of the self-calibration is to determine any changes in the behavior of the instrument and to update the calibration coefficients derived from the ground calibration on Earth accordingly. Figure 5 shows a flow diagram showing the different data sets and intermediate calibration coefficients and the equations used to derive them. The left group shows the main path to the data inversion coefficients, while the right group represents a less accurate determination of sensor sensitivity, which is currently only used to monitor the health of the sensors. Only in case a severe sensor degradation occurs these coefficients would be used to update the calibration coefficients used for inversion.

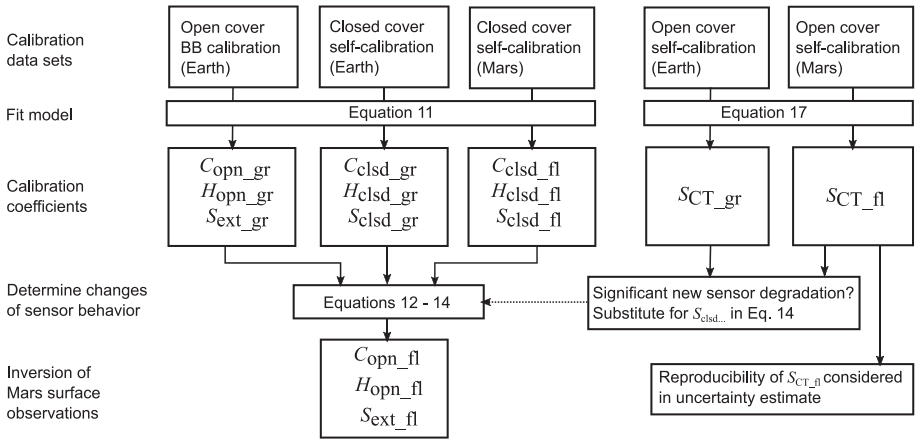

Figure 5. Flow diagram showing the different data sets and the path to derive the set of calibration coefficients used to invert the HP^3 RAD observations acquired on Mars. The different sets of calibration coefficients are identified by abbreviated subscripts: opn—open cover, clsd—closed cover, gr—ground calibration, fl—self-calibration on Mars, ext—sensitivity to external radiation, and CT—sensitivity to open calibration target. Not shown is the dependence of equation (17) on the $H_{\mathrm{opn\_fl}}$ coefficient.

The data from the ground tests observing the cavity blackbody and all the data observing the closed CT are evaluated by fitting equation (11) using linear regression with two independent variables, P_{SH} and F, as described in the work of Press et al. (1992). P_{SH} is given by equation (6), and F is given by equation (10), in which T is substituted by either T_{BB} or T_{CT}. The uncertainty of the fitted parameters is derived by assuming that the errors of the observed voltages correspond to the root of the mean of squared differences between data and fitted model (Press et al., 1992).

The different calibration configurations and tests require different coefficients, indicated by a subscript. An overview is provided in Figure 5. These are S_{ext} for the sensitivity to heat flux from outside of the instrument, S_{clsd} for the sensitivity to heat flux between sensor and the closed CT, and S_{CT} for the sensitivity to the CT in its open state. For all three sensitivity values we use the same calculation of F (equation (10)) with the same parameters assuming the FOV as a cone with half angle of $\vartheta_a = 10°$. This corresponds to the closed cover seen through the SH aperture, while the view factors of the CT aperture and the open CT are smaller. Therefore, the derived sensitivities are different from each other with $S_{\mathrm{clsd}} > S_{\mathrm{ext}} > S_{\mathrm{CT}}$. Similarly, voltage offset C and heater induced offset coefficient H are different for the open and closed state so we use different coefficients, C_{clsd}, H_{clsd}, C_{opn}, and H_{opn}.

In addition to these differences, we observe changes in the coefficients between the Earth and Mars observation; thus, they are each further distinguished with a subscript of "_gr" and "_fl," respectively. The Mars data is inverted to surface brightness temperature using the set of calibration coefficients $C_{\mathrm{opn\_fl}}$, $H_{\mathrm{opn\_fl}}$, and $S_{\mathrm{ext\_fl}}$ to derive the net radiative heat flux F in equation (11) from measured thermopile voltage U_{TC} and SH heater power P_{SH} and then to find the temperature T in equation (10) that provides a matching F at the current sensor temperature T_{ref}. More details are in section 3.4.

3.3.1. Offsets

The coefficient H describing the offset caused by SH heater power P_{SH} is a function of instrument temperature as well as the geometric configuration of the instrument. This parameter, determined before and after shock and vibration tests of the radiometer, showed changes. We interpret this as a sign that it is very sensitive to thermal contacts within the instrument, for example, the contact of the thermopile package walls with the aluminum SH, which could be affected by the mechanical stresses of launch and landing.

Figure 6 shows all thermopile voltages acquired during calibration on Earth and closed cover calibration on Mars, corrected for net radiative heat flux by subtracting the SF term that has been fitted to the corresponding data. Also plotted are the linear fits of this offset voltage as a function of SH heater power that correspond to the derived C and H calibration coefficients. The linear fits describe the observations to within $\approx 4\,\mu$V. The largest scatter is observed in the Mars data and shows signs of hysteresis. Especially, the night data (blue plus symbols) appear in two distinct branches that can be attributed to different local times or more

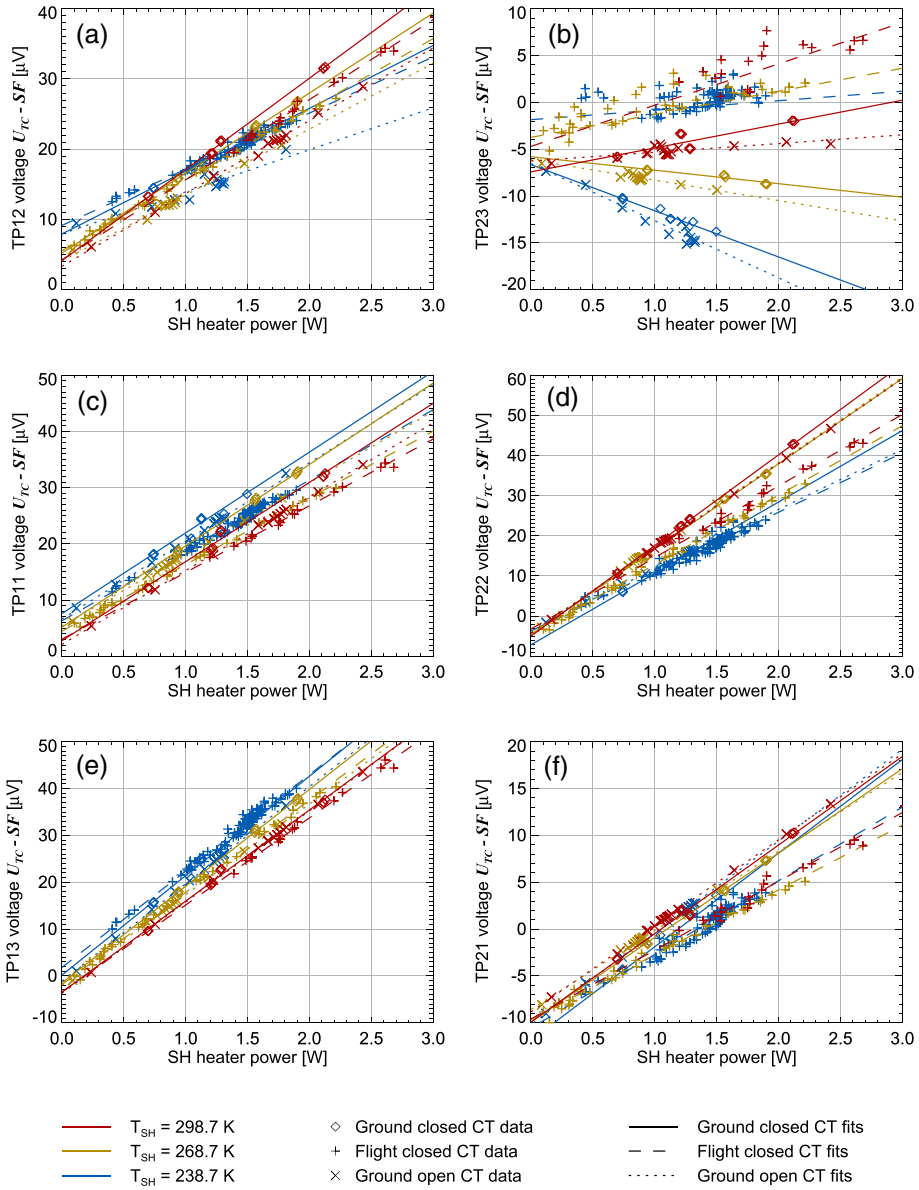

Figure 6. Ground tests and measurements on Mars with the dust cover closed provide data with defined net radiative heat flux on the sensor. Shown are thermopile voltages with radiative heat flux contributions subtracted and fits to thus corrected data as linear functions of RAD SH heater power. (a, c, and e) FOV 1 and (b, d, and f) FOV 2. (a, b) 8–14 μm, (c, d) 8–10 μm, and (e, f) 15–19 μm.

exactly to the environmental temperature change rate. The ground calibration data were not acquired at systematically varying environmental temperature change rates, so we make no attempt to further correct for this hysteresis and instead include the 4 µV in the uncertainty calculation.

There is some regularity to the behavior with respect to instrument temperature, configuration, and location that is more discernible in a plot of the H coefficients versus the instrument temperature shown in Figure 7. The response to heaters H of the two broadband sensors is somewhat linear with respect to instrument temperature, while the narrowband, shorter- and longer-wavelength sensors show more complex behavior (Figures 7c–7f). Together with the unexpected nonlinear behavior of sensitivity described in the next section might be an indication that for narrowband sensors the effects H and S have not been completely disentangled.

The closed cover calibration $H_{\mathrm{clsd\_gr}}$ coefficient is almost always 1 to 2 µV/W larger than the open cover coefficient $H_{\mathrm{opn\_gr}}$ at the same instrument temperature, the sole exception being the Sensor TP22

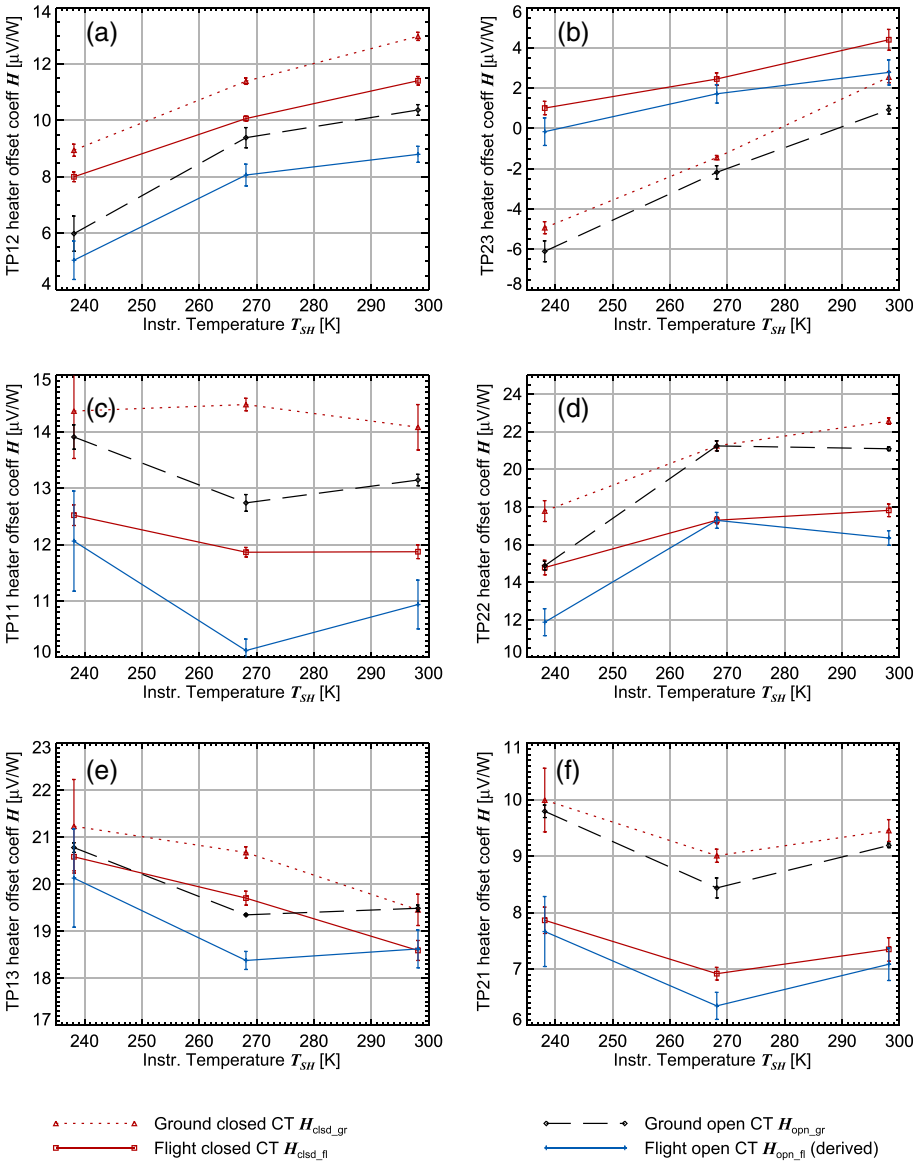

Figure 7. The coefficients of response to SH heater power for each sensor. (a, c, and e) FOV 1 and (b, d, and f) FOV 2. (a, b) 8–14 μm, (c, d) 8–10 μm, and (e, f) 15–19 μm.

at $T_{\text{ref}} = 268.8$ K (Figure 7d). In the two broadband sensors (Figures 7a and 7b) this difference is almost the same for the different instrument temperatures, suggesting that this is mostly a geometrical effect of how the heat from the heaters flows through the SH. In most of the sensors the response to heaters with the closed cover is approximately 1 to 2 µV/W lower on Mars ($H_{\text{clsd\_fl}}$) than in the calibration facility ($H_{\text{clsd\_gr}}$), with little changes between the different temperature set points. The most notable exception is the broadband sensor of FOV 2 (Figure 7b), where $H_{\text{clsd\_fl}}$ is larger at all instrument temperatures and the difference decreases systematically with instrument temperature.

The parameters used to invert the actual Mars surface observations, that is, $C_{\text{opn\_fl}}$ and $H_{\text{opn\_fl}}$, cannot be directly derived due to the unknown temperature of the Mars surface in view of the sensors when the cover is open. This is not the case for the calibration with cover closed that were performed after landing, which yield the coefficients $C_{\text{clsd\_fl}}$ and and $H_{\text{clsd\_fl}}$. We use the difference between the open and closed cover coefficients observed on Earth to derive the open cover coefficients for Mars:

$$C_{\text{opn\_fl}} = C_{\text{clsd\_fl}} + C_{\text{opn\_gr}} - C_{\text{clsd\_gr}} \tag{12}$$

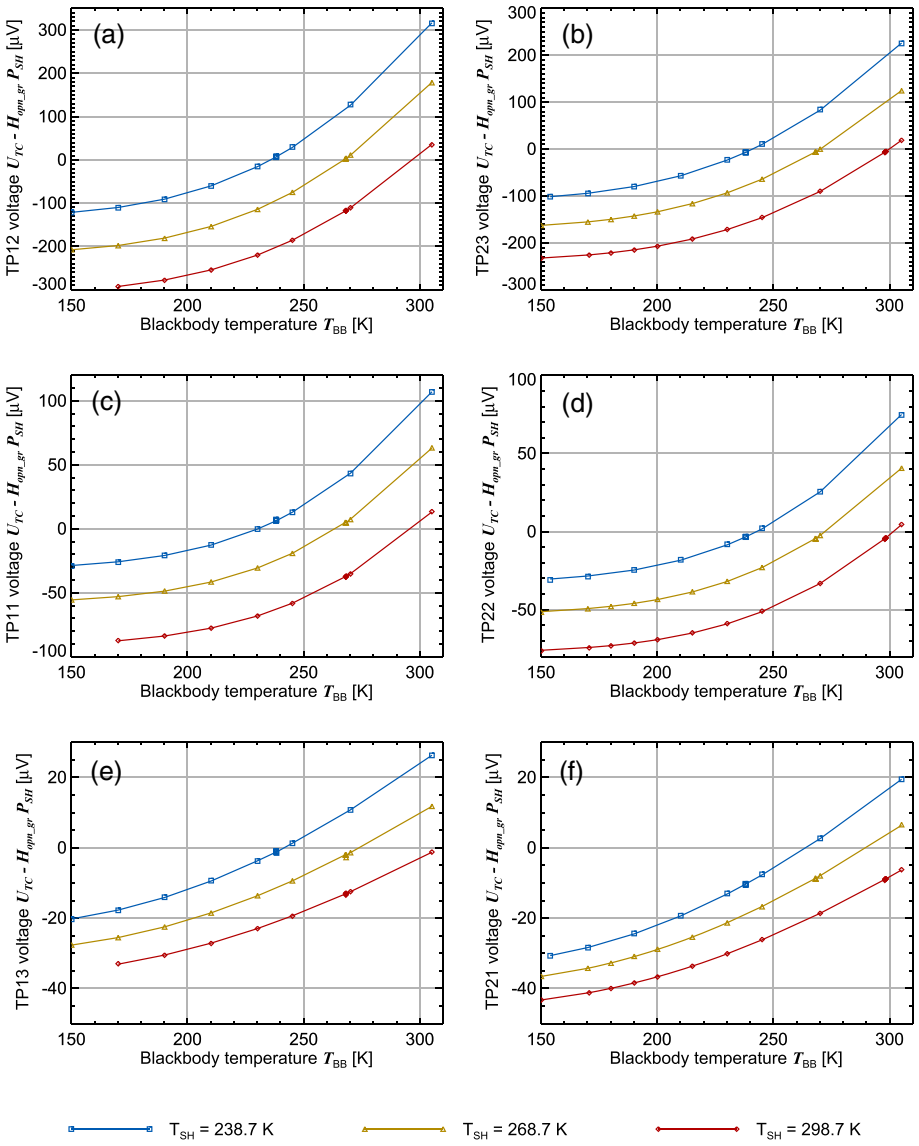

Figure 8. The ground tests provided thermopile voltages at known observed brightness temperatures. Shown here are the heater offset corrected voltage data and the data fit with the derived sensitivity $S_{\text{ext\_gr}}$. (a, c, and e) FOV 1 and (b, d, and f) FOV 2. (a, b) 8–14 μm, (c, d) 8–10 μm, and (e, f) 15–19 μm.

$$H_{\text{opn\_fl}} = H_{\text{clsd\_fl}} + H_{\text{opn\_gr}} - H_{\text{clsd\_gr}}. \tag{13}$$

The errors of these derived coefficients are calculated by adding up the squared individual errors and taking the root. The different error contributions to the total uncertainty of brightness temperature are discussed in section 3.4.

3.3.2. Sensitivity

The data of the calibration using the cavity blackbody are shown in Figure 8, with the respectively fitted offset term $C_{\text{opn\_gr}} + H_{\text{opn\_gr}}\ P_{\text{SH}}$ subtracted. The remaining offset between the curves is due to the different instrument temperatures, T_{ref} in equation (10). The data can be fitted well with the modeled net radiative flux (equation (10)), typically to within 1 µV. The data of the self-calibration and fits to the data are shown in Figure 9. The data can be fitted similarly well as the cavity blackbody, with exception of the calibration data from Mars, which might be an effect of the aforementioned hysteresis in the heater offset.

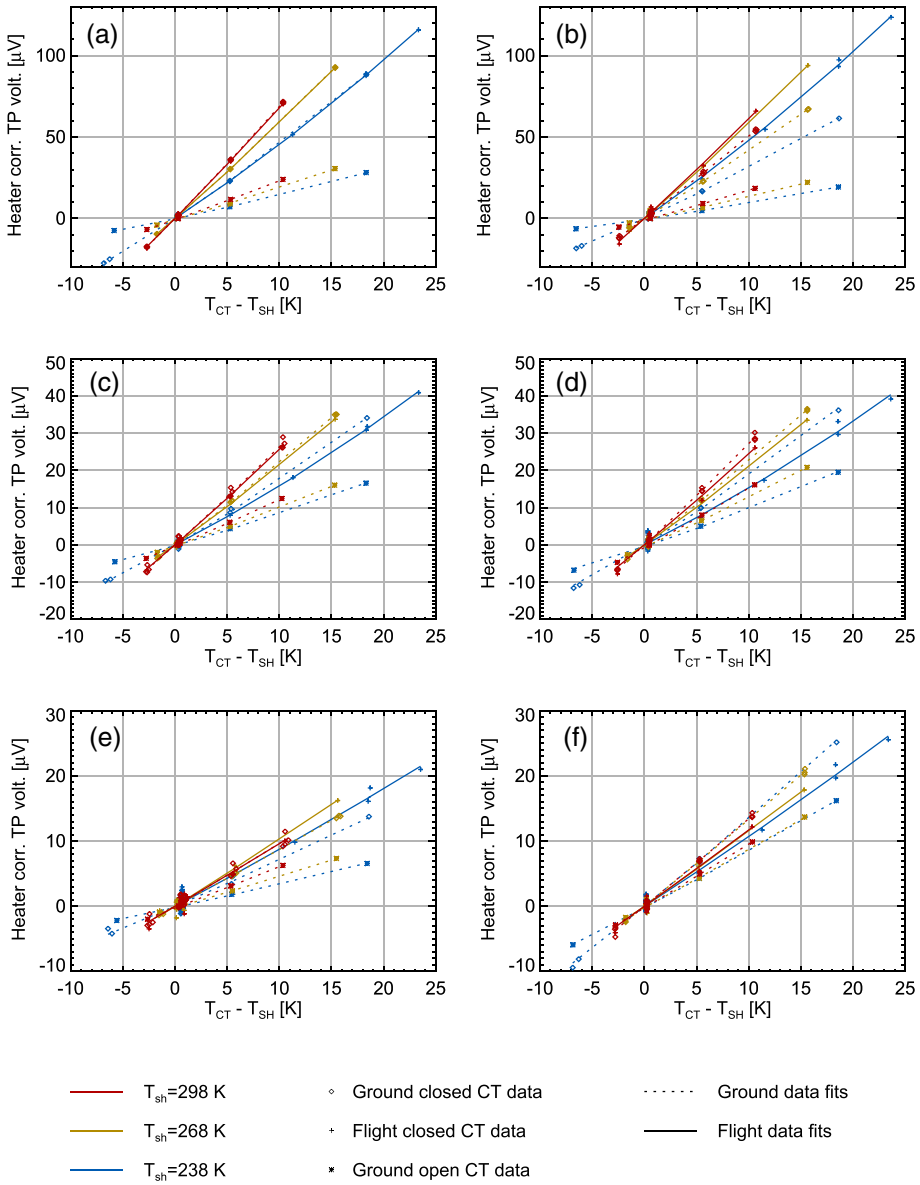

Figure 9. The CT provides a variation of net radiative heat flux that can be measured by the thermopiles. Shown here is the term proportional to S of equation (11), that is, the measured thermopile voltage corrected for the heater offset and the background in case of the open cover data. (a, c, and e) FOV 1 and (b, d, and f) FOV 2. (a, b) 8–14 µm, (c, d) 8–10 µm, and (e, f) 15–19 µm.

The fitted sensitivities are shown in Figure 10 as a function of instrument temperature. The coefficients S_{ext_gr} decrease by ≈ 0.5% per K of instrument temperature, as expected due to the increase of sensor fill-gas thermal conductivity with temperature. The closed cover coefficients S_{clsd_gr} and S_{clsd_fl} show a less clear linear behavior, except in the two broadband sensors (Figures 10a and 10b). As mentioned before, the heater offset coefficients H for the narrowband sensors also change less systematically with instrument temperature than for the broadband sensors. The signal of the narrowband sensors are only 50% to 20% of that of the broadband sensors, and the offset voltages generated by the heaters are of the same order of magnitude or even larger than the signal of the self-calibration measurements (cf. Figure 6 with Figure 9). Considering that a linear trend of sensitivity with respect to instrument temperature is the nominal behavior of the sensors, it is likely that this fit does not completely disentangle the external radiative heat flux from the thermal state of the instrument in case of the narrowband sensors.

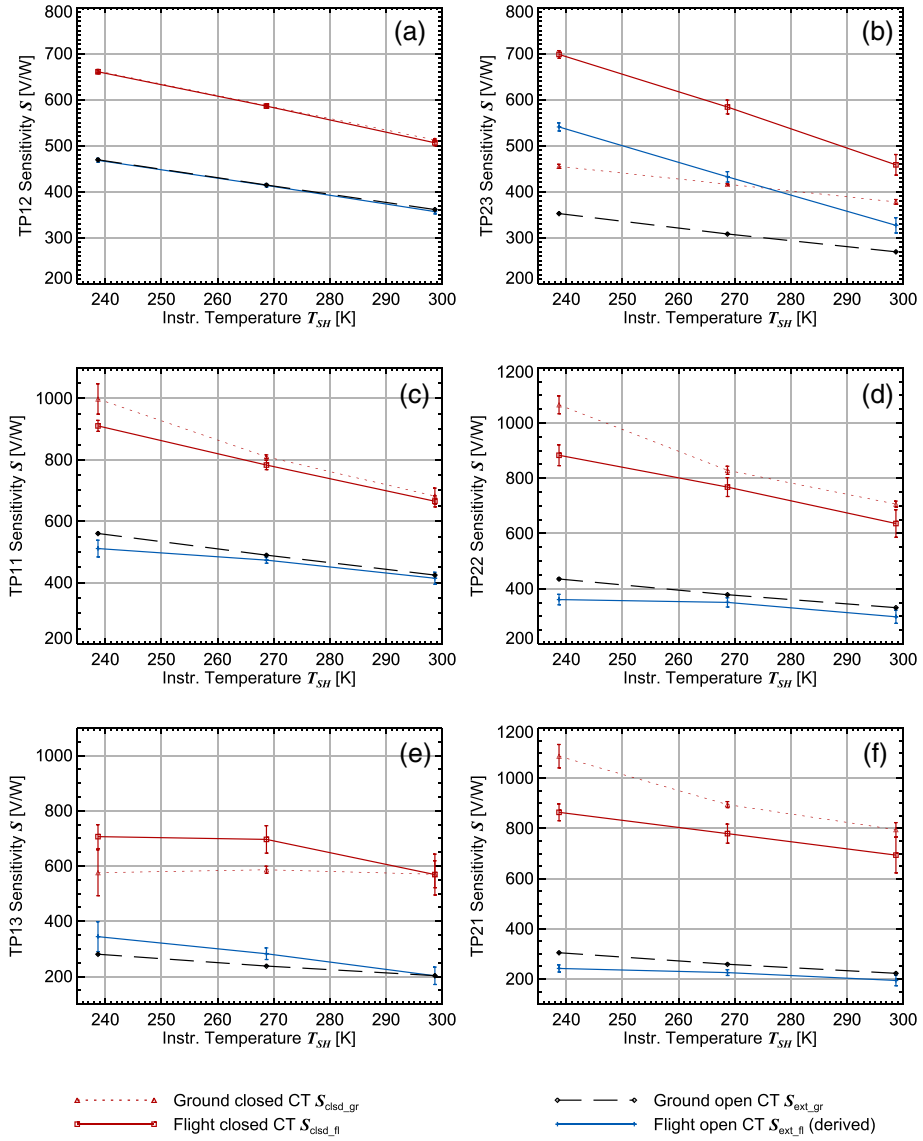

Figure 10. The sensitivity S derived from various calibrations. Dotted black line is from the ground calibration using the external blackbody $S_{\text{ext\_gr}}$. Dotted red line is from the closed cover internal calibration on Earth $S_{\text{clsd\_gr}}$. Solid red line is from the closed cover internal calibration on Mars $S_{\text{clsd\_fl}}$. Solid blue line is the sensitivity $S_{\text{ext\_fl}}$ used to invert Mars surface data, derived from the other three sensitivities using equation (14). (a, c, and e) FOV 1 and (b, d, and f) FOV 2. (a, b) 8–14 μm, (c, d) 8–10 μm, and (e, f) 15–19 μm.

The change of $S_{\text{clsd\_fl}}$ relative to $S_{\text{clsd\_gr}}$ gives the best evidence of changes in the sensor and thus is used to update $S_{\text{ext\_gr}}$ to provide the sensitivity used to invert Mars surface data:

$$S_{\text{ext\_fl}} = S_{\text{ext\_gr}} \frac{S_{\text{clsd\_fl}}}{S_{\text{clsd\_gr}}}. \tag{14}$$

The relative error for this derived sensitivity is calculated by from the square root of the sum of variances corresponding to the relative errors of the individual contributions.

The FOV 1 broadband sensors shows the same sensitivity to the closed dust cover both on Earth ($S_{\text{clsd\_gr}}$) and Mars ($S_{\text{clsd\_fl}}$) (Figure 10a). Accordingly, the sensitivity used to invert the data on Mars $S_{\text{ext\_fl}}$ is very similar to that derived from the cavity blackbody measurements $S_{\text{ext\_gr}}$, even though the heater offset is different. The FOV 2 broadband sensor shows for the 238.7-, 268.7-, and 298.7-K set points an increase in closed cover sensitivity on Mars of 53%, 40%, and 21%, respectively, relative to the Earth calibration. The corresponding

S_{ext_fl} is in the same range as that of the FOV 1 broadband sensor and within expectations for the sensor design.

The new sensitivity of the FOV 2 broadband sensor is still close to a linear function with respect to instrument temperature, but the gradient is with −0.8%/K higher than in the ground calibration (−0.3%/K), and approximately twice as high as that of the FOV 1 broadband sensor. The higher sensitivity could indicate that the heat transfer between the hot and cold junctions of the sensors thermocouples has decreased overall. The higher gradient of sensitivity with respect to instrument temperature could indicate a higher relative contribution of heat conduction through the sensor fill-gas, consistent with a reduction of the heat conducted through the solid portions of the sensor.

3.3.3. Sensor Stability

In order to evaluate whether the sensitivity of the sensors evolves further, for example, by deposition of dust on the sensor windows, we observe the response of the sensors to temperature variation of the CT in its open state, parameterized by the sensitivity S_{CT}. For the determination of S_{CT}, the equation describing the observed voltage (equation (11)) requires another term because in addition to the net heat flux from the CT partially in the FOV F_{CT}, there is net heat flux from the surface F_{ext} reaching the sensor through the aperture of the CT:

$$U_{TC} = C_{opn} + H_{opn}P_{SH} + S_{CT}F_{CT} + S_{ext}F_{ext}. \tag{15}$$

In ground calibration tests, F_{ext_gr} is a known quantity derived from the blackbody temperature, but on Mars this has to be constrained by other means.

To do so, we need for each calibration point (defined by one set of P_{SH}, F_{CT}, F_{ext}, and U_{TC}) a matching reference set (P'_{SH}, F'_{CT}, F'_{ext}, and U'_{TC}) for which it can be assumed that the associated external background heat flux is the same:

$$F'_{ext} = F_{ext}. \tag{16}$$

This series of reference points is derived by interpolation between the calibration set points with nominally no temperature difference between SH and CT, that is, the first, fourth, and sixth set point in the calibration sequence (Table 1). Interpolation is done by matching the values of P_{SH}, F_{CT}, and U_{TC} each with a second-degree polynomial as function of time at these three set points, and then evaluating the polynomials at the times of all six set points to calculate sets of P'_{SH}, F'_{CT}, and U'_{TC}. Substituting in and then subtracting from equation (15) yields

$$U_{TC} - U'_{TC} = S_{CT}(F_{CT} - F'_{CT}) + H_{opn}(P_{SH} - P'_{SH}). \tag{17}$$

This equation is then fitted to the data to determine S_{CT}, using the offset coefficients calculated as described in section 3.3.1, that is, H_{opn_gr} for the ground calibration and H_{opn_fl} for Mars data. The ground calibration data and its fit is presented in Figure 9. The resulting fitted sensitivities are shown in Figure 11.

On Mars, this procedure of using three set points of the calibration sequence for background interpolation can only be applied to the day time calibration set points. In case of the nighttime instrument temperature set point, T_{SH} = 238.7 K, technical issues required a different calibration sequence (see Table 1). Instead we assume that sol-to-sol variability of surface temperature at the same local solar time is small and use normal measurements (which also have $T_{CT} = T_{SH}$) as close in time as possible to interpolate to the local solar times of calibration measurements. The resulting values are indicated by "×" symbols in Figure 11. In case of the T_{SH} = 298.7 K set point it is possible to employ both approaches after Sol 100. The results of the two methods are consistent within 10% for the broadband sensor in FOV 1 (TP12) and to within 5% for the broadband sensor in FOV 2 (TP23). The average sensitivity of the different calibration runs and their standard deviation is given in Table 3.

For the two broadband sensors the results are roughly consistent with the behavior observed with the CT closed. The FOV 1 broadband sensor shows sensitivities consistent with ground calibration values, with a reproducibility of 1–2% for the T_{SH} = 268.7 K set point. The T_{SH} = 298.7 K values show greater variability but this is expected because this calibration either occurs in the late afternoon, when the high power

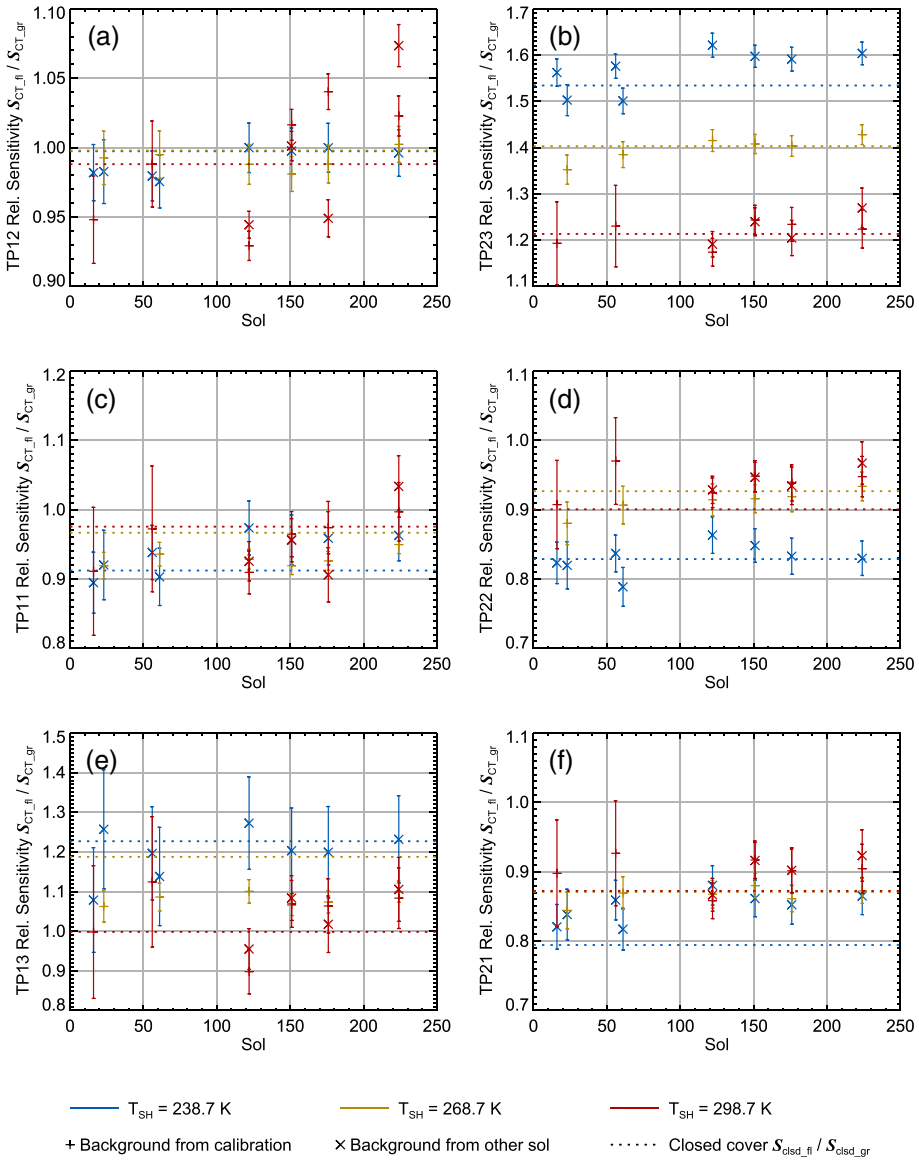

Figure 11. The sensitivity to the open CT S_{CT_fl} derived from various calibrations on the surface of Mars presented in relative to the ground calibration values S_{CT_gr}. Two different methods of background correction are applied as described in the text. (a, c, and e) FOV 1 and (b, d, and f) FOV 2. (a, b) 8–14 μm; (c, d) 8–10 μm, and (e, f) 15–19 μm.

required to heat the instrument against the environment causes larger uncertainty, or close to noon, when the atmosphere is more turbulent.

The FOV 2 broadband sensor shows an increase of sensitivity consistent with that observed with the closed cover (Figure 11b). The 238.7-K set point sensitivity increased somewhat more than in the closed cover calibration; however, there are some indications that this set point is systematically impacted by hysteresis of the heater correction and possibly by the background. In the calibrations before Sol 100 the 238.7-K calibration is preceded directly by either the 268.7 K or the 298.7-K calibration, and the results seem to depend on which of the two. After Sol 100 it is always the 268.7-K set point preceding the 238.7-K calibration, but the background correction might be affected by the hysteresis. The time of switching from the day temperature set point to the night set point was moved 1 hr earlier to 17 hr LTST around Sol 120 so that the instrument experienced different thermal histories prior to the local time of calibration before and after this date. The other sensors show open cover sensitivities mostly consistent with the closed cover measurements; however, the uncertainties are large and the behavior with instrument temperature appears erratic so that few conclusion can be drawn from that.

Table 2
Parameters Used for Calibration of Data Acquired on Mars for All Six Thermopiles

	TP11	TP12	TP13	TP21	TP22	TP23
			Offset voltage C_{opn_fl} (μV)			
c	5.31 ± 0.74	9.15 ± 0.73	0.50 ± 0.88	−8.88 ± 0.54	0.25 ± 0.70	−1.74 ± 0.73
w	4.65 ± 0.22	4.40 ± 0.39	−2.36 ± 0.23	−8.32 ± 0.25	−4.10 ± 0.45	−4.06 ± 0.48
h	2.36 ± 0.59	3.42 ± 0.46	−3.68 ± 0.62	−8.50 ± 0.48	−2.49 ± 0.71	−3.54 ± 1.13
			Sensitivity S_{ext_fl} (V/W)			
c	510.8 ± 13.7	468.1 ± 2.2	344.3 ± 27.0	242.1 ± 7.0	360.6 ± 9.5	540.7 ± 4.4
w	473.1 ± 5.0	413.7 ± 1.7	282.5 ± 10.5	225.4 ± 5.7	350.5 ± 8.4	432.3 ± 5.6
h	414.0 ± 9.8	356.8 ± 2.5	202.6 ± 15.8	194.2 ± 10.5	298.3 ± 11.9	326.9 ± 8.3
			Response to heater power H_{opn_fl} (μV/W)			
c	12.06 ± 0.89	5.04 ± 0.68	20.13 ± 1.04	7.66 ± 0.62	11.88 ± 0.72	−0.16 ± 0.69
w	10.12 ± 0.20	8.06 ± 0.39	18.38 ± 0.19	6.34 ± 0.24	17.29 ± 0.42	1.72 ± 0.46
h	10.94 ± 0.43	8.80 ± 0.28	18.63 ± 0.40	7.08 ± 0.29	16.36 ± 0.39	2.78 ± 0.62

Note. The first column indicates temperature set point. c: 238.7 K, w: 268.7 K, and h: 298.7 K.

3.4. RAD Data Inversion and Uncertainty

Brightness temperatures T_B are derived from equation (10) by taking $\varepsilon = 1$ and linearly interpolating between net flux values calculated in intervals of 1 K to calculate the temperature that matches the F value corresponding to the measured thermopile voltage corrected for offsets (C_{opn_fl} and $H_{opn\_fl}P_{SH}$) and sensor sensitivity (S_{ext_fl}) in equation (11). Brightness temperature errors are derived from the partial derivatives of the above inversion $T_B(U_{TC}, P_{SH}, C_{opn\_fl}, H_{opn\_fl}, S_{ext\_fl})$ calculated using finite differences. The kinetic temperatures T are calculated by assuming an emissivity of 0.98 ± 0.02 (Morgan et al., 2018).

The total uncertainty is calculated by taking the root of the sum of variances of the different error contributions. The thermal and electronic noise of the thermopile voltage is 100 to 1,300 nV. For calibration measurements this is negligible since it is efficiently reduced by averaging over at least 23 measurements. The largest observed fit residual during the closed cover calibration is 4 μV, which we attribute to a hysteresis with respect to the thermal environment. We therefore take $\Delta U_{TC} = 4\,\mu V$ and assume that this describes an interval of uniform error distribution and take the corresponding variance as $1/3\ \Delta U_{TC}^2$, consistent with the recommendations of the GUM (2008) for maximum errors. The maximum error observed in the heater power is provided in equation (7), with corresponding variance being $1/3\ \Delta P_{SH}^2$.

The errors for the calibration coefficients are given in Table 2. The estimate of sensitivity uncertainty pertains however to the moment of closed cover calibration, and there is a concern that sensitivity evolves further, for example, due to dust deposition on the filter windows. The ongoing calibrations do not indicate a clear trend (Figure 11); however, we cannot exclude an additional sensitivity drift due to the insufficient reproducibility of the open cover calibration, as represented by the standard deviations in Table 3.

Table 3
Average of Sensitivity to the Open Calibration Target S_{CT_fl} and Its Standard Deviation σS_{CT_fl} in Units of V/W for the Different Self-Calibration Runs Up to Sol 250

	TP11	TP12	TP13	TP21	TP22	TP23
c ($N = 8$)	463.8 ± 14.5	209.5 ± 2.1	347.5 ± 18.4	596.9 ± 15.6	485.1 ± 12.8	229.9 ± 6.6
w ($N = 6$)	353.2 ± 4.4	195.6 ± 1.4	352.4 ± 5.4	520.5 ± 7.4	445.6 ± 8.6	199.3 ± 3.8
h ($N = 6$)	308.6 ± 11.7	176.0 ± 7.8	390.8 ± 30.2	522.1 ± 13.6	389.6 ± 9.0	167.0 ± 3.7

*Note.*The c indicates the 238.7-K set point, the w the 268.7-K set point, and the h the 298.7-K set point.

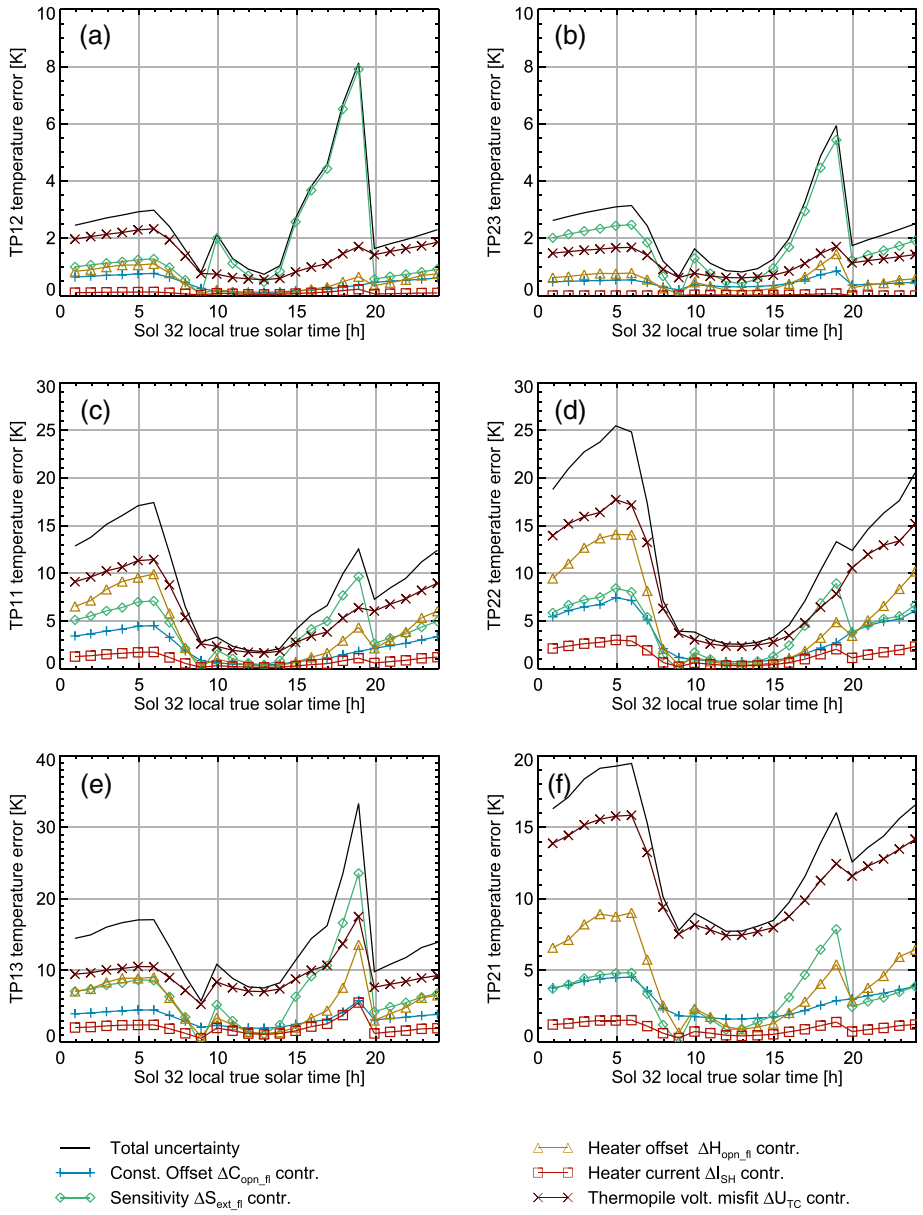

Figure 12. RAD inverted data uncertainty budget as a function of local time. The different graphs correspond to the different terms contributing to equation (18). (a, c, and e) FOV 1 and (b, d, and f) FOV 2. (a, b) 8–14 μm, (c, d) 8–10 μm, and (e, f) 15–19 μm.

We therefore include the standard deviation of the open cover calibration results ($\sigma S_{\mathrm{CT\_fl}}$) in the error budget. Together the uncertainty of brightness temperature ΔT_{B} is

$$\Delta T_{\mathrm{B}} = \left[\left(\frac{\mathrm{d}T_{\mathrm{B}}}{\mathrm{d}C}\Delta C_{\mathrm{opn\_fl}}\right)^2 + \left(\frac{\mathrm{d}T_{\mathrm{B}}}{\mathrm{d}H}\Delta H_{\mathrm{opn\_fl}}\right)^2 + \left(\frac{\mathrm{d}T_{\mathrm{B}}}{\mathrm{d}S}\Delta S_{\mathrm{ext\_fl}}\right)^2 + \left(\frac{\mathrm{d}T_{\mathrm{B}}}{\mathrm{d}S}\frac{\sigma S_{\mathrm{CT\_fl}}}{S_{\mathrm{CT\_fl}}}S_{\mathrm{ext\_fl}}\right)^2 + \left(\frac{\mathrm{d}T_{\mathrm{B}}\Delta I_{\mathrm{PSH}}}{\mathrm{d}I_{\mathrm{PSH}}\ 3}\right)^2 + \left(\frac{\mathrm{d}T_{\mathrm{B}}\Delta U_{\mathrm{TC}}}{\mathrm{d}U_{\mathrm{TC}}\ 3}\right)^2 \right]^{\frac{1}{2}}. \quad (18)$$

The resulting uncertainty and different contribution of all sensors are shown in Figure 12 for Sol 32, during which the set point of $T_{\mathrm{SH}} = 298.7$ K is used between 10 and 19 hr LTST. The two contributions from sensitivity uncertainty are combined since they behave identically with local time. The sensitivity dominates the total uncertainty of the broadband sensors (Figures 12a and 12b) in the afternoon. This is a consequence of the large difference between instrument temperature and observed temperature. At night, the uncertainty

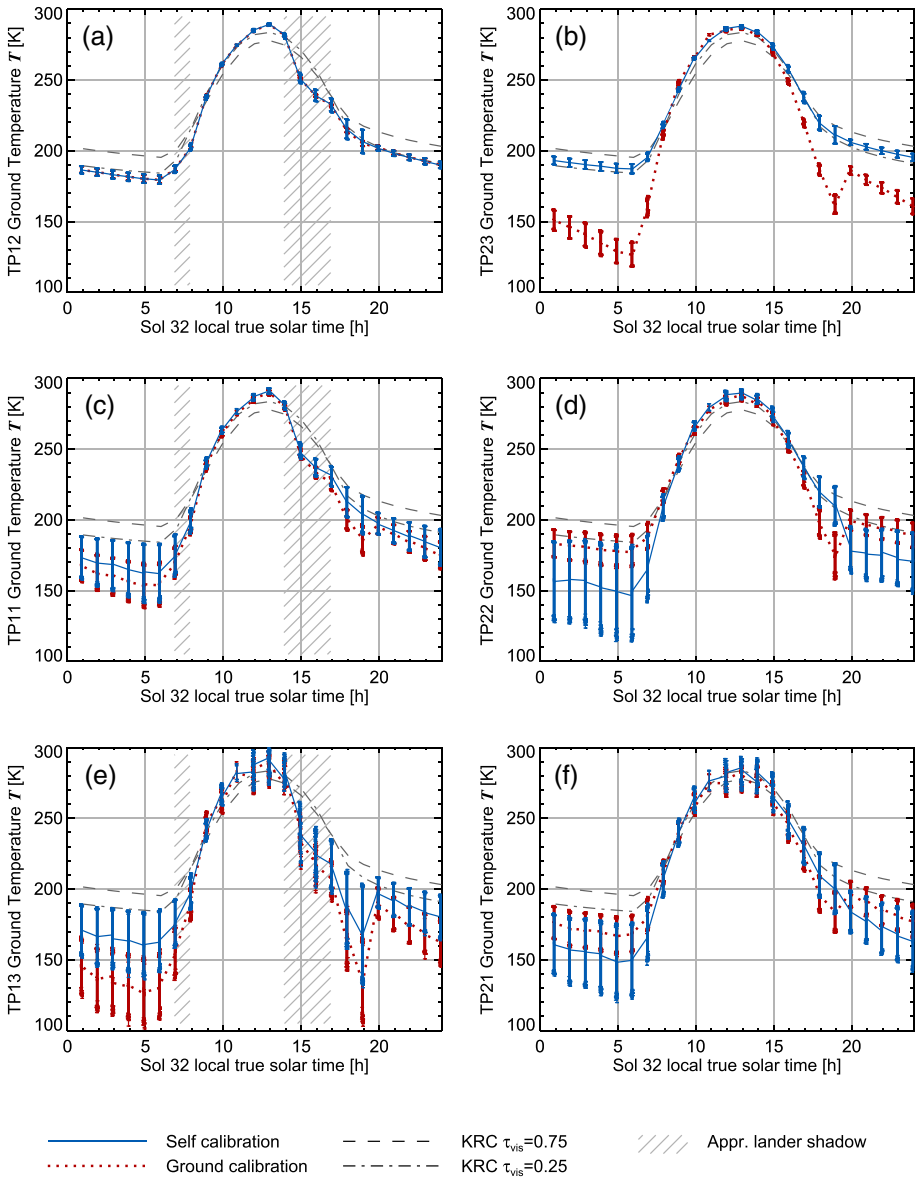

Figure 13. RAD measurements inverted with two different sets of calibration coefficients for each of the sensors. Plotted in red are the data inverted with the original calibration on the ground, and plotted in blue are the data inverted with the calibration coefficients updated with the self-calibration. Switches between the "hot" and "cold" instrument temperature set points occurred before the 10 and 19 hr local times. KRC model curves and lander shadowing are described in the text. (a, c, and e) FOV 1 and (b, d, and f) FOV 2. (a, b) 8–14 μm, (c, d) 8–10 μm, and (e, f) 15–19 μm.

of the thermopile voltage that we attribute to thermal hysteresis is the most or second most important error source for the broadband filters. For the narrowband filters the contribution of the heater induced offset is also significant.

Figure 13 shows for comparison the data inverted with the ground calibration coefficients and with the updated calibration coefficients. As a reference we also provide diurnal curves calculated with a thermal model (KRC Kieffer, 2013) that has been developed to derive thermophysical properties of the Mars surface from orbiter observations. The reference curves are calculated for a flat surface at a latitude of 4.3° and a solar longitude of 313°, approximately corresponding to 29 December of 2018, when the data in Figure 13 have been acquired. For the thermophysical parameters we chose the thermal inertia of 200 Jm^{-2} K^{-1} $s^{-1/2}$ and an albedo of 0.24, which Golombek et al. (2017) provide as averages for the InSight landing ellipse based on THEMIS observations (Fergason et al., 2006) and TES observations (Christensen et al., 2001; Putzig et

al., 2005), respectively. For the visible wavelengths atmospheric dust opacity we chose a range of 0.25 to 0.75, which approximately represents the uncertainty of the this parameter as it is derived from the Lander Instrument Context Camera in this period of the mission (Banfield et al., 2020). Thermophysical parameters are set as independent of temperature. The other parameters of the model are the same as in the input file provided in section S8 of the work of Kieffer (2013). The resulting two diurnal curves are plotted in each panel of Figure 13.

The temperature data from the broadband sensors (Figures 13a and 13b) match the KRC curves well. Differences could be related to local differences of albedo and other thermophysical properties from those used in the model, and the effect of the InSight lander itself. Golombek et al. (2020) report that the thermal inertia indicated by the FOV 2 broadband sensor data is in the range of 160 to 230 $Jm^{-2}\ K^{-1}\ s^{-1/2}$. The dust cover near the lander has been disturbed by the landing rockets, reducing the albedo by approximately 35% (Golombek et al., 2020). The spot observed by RAD FOV 1 in approximately 0.5-m distance from the lander deck (see Figure 11 in Spohn et al., 2018) is affected by solar panel shadows passing through in the morning and afternoon Figure 13 shows the periods of shadowing based on the nominal lander orientation and distance to the surface, which are approximately the same as the actual values. In addition to the shadowing, a significant fraction of the sky seen from the closer spot is obscured by the lander so that lander emission and reflection might be significant for the surface energy budget.

The near spot broadband sensor (Figure 13a) shows little difference between the original calibration and the updated calibration, as expected, while the far spot broadband sensor (Figure 13b) clearly shows the effect of the changed sensitivity. The sensors with narrow spectral band filters (Figures 13c–13f) show larger differences between the two sets of calibration coefficients, which are mostly consistent with the larger uncertainties of these coefficients. The FOV 1 long-wavelength sensor (Figure 13e) and the FOV 2 short-wavelength sensor (Figure 13d) show evidence of significant errors in one or more of the calibration coefficients even after application of the self-calibration, indicated by the discontinuity of the data at the time when the instrument temperature set point was changed between 19 and 20 hr LTST.

All the narrowband sensors also deviate from the broadband sensor brightness temperatures at night for values approximately equivalent to 1σ of the calibration uncertainty. The narrowband sensors show brightness temperatures at night that are lower those of the broadband sensors, while the day-time temperatures do not show such a systematic deviation. Aside from calibration errors, such differences between brightness temperatures at different bands could be either due variations in the emissivity spectrum or heterogeneous temperatures within each FOV. In case of different effective emissivities in the different bands, there would be differences in brightness temperatures over the whole temperature range, while the observations show good agreement at noon. The temperature heterogeneity can expected to be largest during the day, when shadows and slopes can cause contrasts in insolation, and smallest at the end of the night, when insolation was zero everywhere for 12 hr. Therefore, neither emissivity variation nor temperature heterogeneity can explain the observed brightness temperature differences between the spectral bands.

The most likely alternative explanation is that the calibration did not completely disentangle the effects of observed flux and the instrument thermal environment, as discussed in section 3.3.2. Unlike the broadband sensors, the narrowband sensors all show lower sensitivity at the 238.7-K instrument set point than could be expected extrapolating from the 268.7- and 298.7-K instrument set points (Figure 10). A 15% to 35% higher sensitivity coefficient in the narrowband sensors would approximately align their calibrated brightness temperature at night with that of the broadband sensors. These numbers would not necessarily be the appropriate corrections, because incorrect sensitivity coefficients could be accompanied by incorrect heater response coefficients and thermopile voltage offsets. It is conceivable that the broadband sensors also suffer from such a systematic calibration error within, resulting in an overestimate of the cooling rates at night, which, however, is unlikely to exceed the 1 σ uncertainty by much.

4. Geometric Calibration

The main objective of the geometric calibration is to verify the designed FOVs of the instrument. The knowledge of the FOVs allows to locate the observed surface in images and stereo topography (Abarca et al., 2019) from the camera mounted on the robotic arm of the InSight lander (Maki et al., 2018). Within the coordinate frame used by the lander, the central azimuth at which the RAD observes is 20° counterclockwise from the x axis, which is aimed to be aligned with North at landing. The central elevation of the two FOVs are at

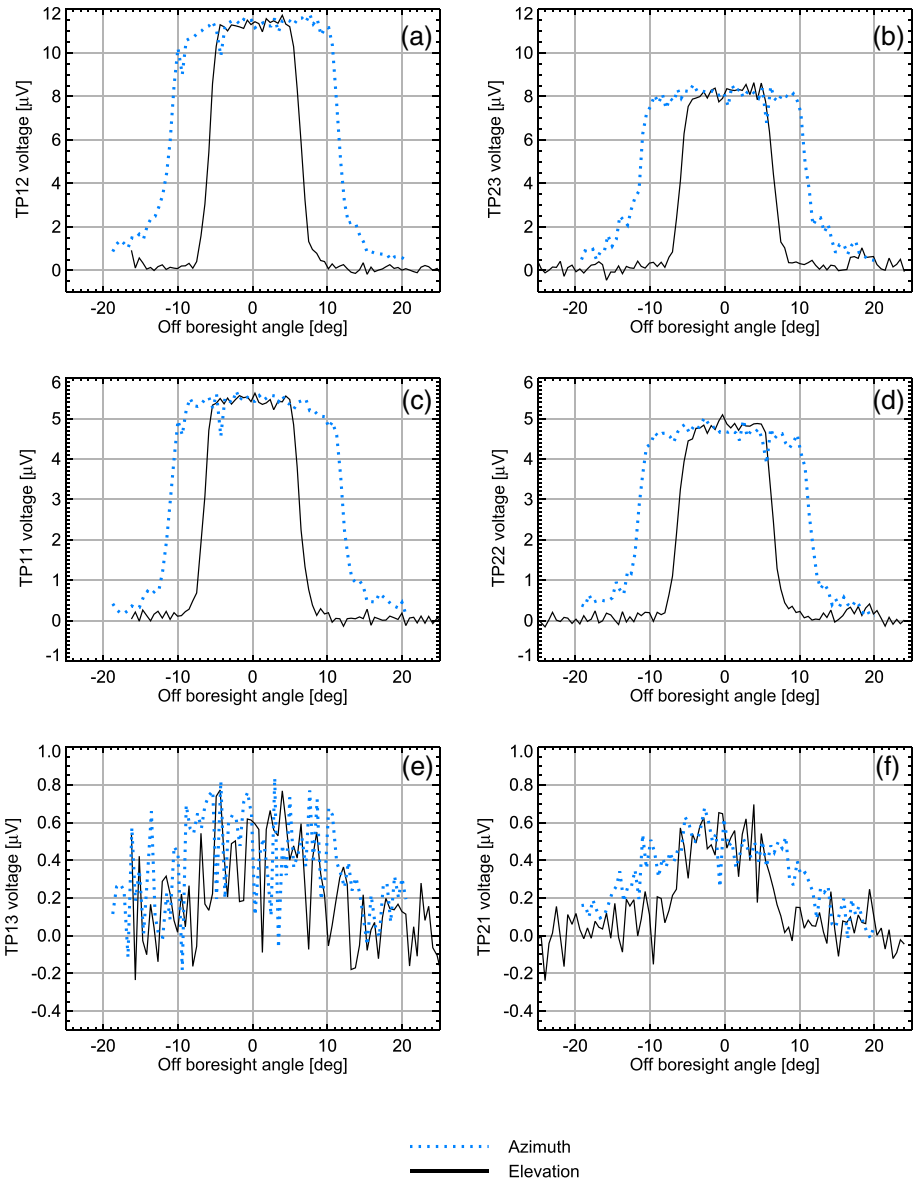

Figure 14. The geometric calibration measurements outline the two fields of view. Shown are the thermopile voltages acquired while observing a collimated, narrow beam at various angles relative to the sensor boresight. The elevation profile is in the plane spanned by the boresight, and the lander deck normal and the azimuth profile is perpendicular to that. The thermopile voltages are corrected for background drift using the radiation source chopper. (a, c, and e) FOV 1 and (b, d, and f) FOV 2. (a, b) 8–14 µm, (c, d) 8–10 µm, and (e, f) 15–19 µm.

−55° and −25° relative to the lander deck. We present the results of the geometric calibration relative to the boresight directions constituted by these azimuth and elevation angles.

Measurements for the geometric calibration were performed in the facilities of the DLR Institute of Optical Sensor Systems, Berlin, Germany. The setup consists of the HP^3 RAD mounted on a pan-tilt unit that can orient the SH at defined angles relative to the collimated beam of an infrared radiation source pointed at the SH. The radiation source is a cavity blackbody at 1000 K equipped with a shutter to allow for differential measurements.

For the geometric calibration, three profiles are acquired. The profiles consist of continuous RAD measurements while either elevation or azimuth is varied with a constant angular velocity and the radiation source shutter alternates between open and closed at approximately 10-s intervals. The first profile is at the azimuth

corresponding the boresight vectors of the sensors and varies elevation from approximately −70° to 0° relative to the lander deck. The other two profiles vary the azimuth from −20° to +20° clockwise at each of the two boresight elevations. The data are corrected for background by subtracting the signal observed with the cavity blackbody shutter closed. The resulting corrected thermopile voltages are shown in Figure 14.

The signal observed by the broadband and short-wavelength sensors is satisfactory; however, the long-wavelength sensors are not well suited to observe the 1000-K radiation source. The signal is largely consistent with the expectations from the instrument design. The SH is designed to geometrically limit the FOV of each sensor to a 20° full width cone around each boresight. The CT further restricts the FOV to ±5° in elevation.

The observed full width at half maximum is approximately 24° in azimuth and 12° in elevation. Negligible signal is received at the range larger than +10° off boresight of FOV 2 in elevation direction, which corresponds to −15° elevation relative to the lander deck. Therefore, there is negligible signal received from the sky.

5. Conclusions

The ground and in situ radiometric calibrations of the HP^3 RAD enable the long term observation of the thermal environment near the InSight lander and thus a constraint on the artificially induced heat flow anomaly. The onboard calibration after landing showed that the broadband sensor observing the nearer spot (TP12) remains unchanged relative to the ground calibration, while the other broadband sensor (TP23) increased in sensitivity by ≈50%. The cause of this increase is unknown but the sensitivity of both sensors now have a similar value that is consistent with expectations for that design. The temperatures observed using the recalibrated sensitivity are consistent with expectations for the observed surface (Golombek et al., 2020).

The resulting temperature uncertainties for the broadband sensors are on the order of 3 K at night for both sensors. There is a brief period in the late afternoon where formal uncertainties can be as large as 6 to 8 K due to the large difference between observed surface temperature and instrument temperature of $T_{\mathrm{SH}} = 298.7$ K, but we do not anticipate that this is a large impediment to the data analysis. The large uncertainty in this period does not seem to be associated with a strong deviation from a plausible diurnal curve. The provided uncertainty is more governed by possible systematic errors, while the the random noise of the instrument is a minor contribution. The noise equivalent temperature difference is less than 0.3 K for the two broadband sensors. Part of the provided uncertainty is the possibility of a slow, ongoing sensor drift that would be so far undetectable using the regular self-calibration, which is reproducible to within 1–2% under the best circumstances.

Systematic errors could potentially be detected in the inverted data in the form of diurnal curve discontinuities at the local times when the instrument temperature is changed, since each instrument temperature is associated with independently derived calibration coefficients. However, this is not observed in the broadband sensors. The narrowband sensors on the other side show some evidence of such discontinuities. The narrowband sensors furthermore show a larger than expected difference to the broadband sensor diurnal curves at night. The most likely explanation is that the calibration coefficients for these sensors have systematic errors somewhat larger than those corresponding to the stated 1σ uncertainty, though not exceeding the 2σ level. The intended use of these sensors was to provide some spectrally resolved information in case that there is a large surface inhomogeneity in the FOV, for example, from larger boulders or pockets of aeolian dust. The InSight landing site is fairly homogeneous and flat, without any clasts larger than 10 cm within the FOVs of RAD (Golombek et al., 2020), so that such information is less useful. The narrowband sensors, however, might still be useful in investigating the temperature response to the lander shadow moving throughout the spot observed by FOV 1.

Acknowledgments
We acknowledge the contribution of the many persons involved in the process of building this instrument, getting it to the surface of Mars, and safely operating it there. The design, building of, and research into the HP^3 has been supported by the German Aerospace Center DLR, United States National Aeronautics and Space Administration NASA, Austrian Academy of Sciences ÖAW, and the Polish Academy of Science CBK PAN. The data acquired during the calibration on Earth and used for this paper are archived on figshare (Mueller, 2019), and the Mars data are archived on the Planetary Data System (Planetary Data System, 2019). This is InSight Contribution Number 137.

References

Abarca, H., Deen, R., Hollins, G., Zamani, P., Maki, J., Tinio, A., et al. (2019). Image and data processing for InSight Lander Operations and Science. *Space Science Reviews*, *215*(2), 22. https://doi.org/10.1007/s11214-019-0587-9

Banerdt, W., Smrekar, S., Banfield, D., Giardini, D., Golombek, M., Johnson, C., et al. (2020). Early results from the InSight mission: Mission overview and global seismic activity. *Nature Geoscience*, *13*, 190–198. https://doi.org/10.1038/s41561-020-0544-y

Banfield, D., Spiga, A., Newman, C., Forget, F., Lemmon, M., Lorenz, R., et al. (2020). First results from InSight's meteorology station on Mars. *Nature Geoscience*, *13*, 183–189. https://doi.org/10.1038/s41561-020-0534-0

Christensen, P. R., Bandfield, J. L., Hamilton, V. E., Ruff, S. W., Kieffer, H. H., Titus, T. N., et al. (2001). Mars Global Surveyor Thermal Emission Spectrometer experiment: Investigation description and surface science results. *Journal of Geophysical Research*, *106*(E10), 23,823–23,872. https://doi.org/10.1029/2000JE001370

Fergason, R. L., Christensen, P. R., Bell, J. F., Golombek, M. P., Herkenhoff, K. E., & Kieffer, H. H. (2006). Physical properties of the Mars Exploration Rover landing sites as inferred from Mini-TES-derived thermal inertia. *Journal of Geophysical Research*, *111*, E02S21. https://doi.org/10.1029/2005JE002583

Fergason, R. L., Christensen, P. R., & Kieffer, H. H. (2006). High-resolution thermal inertia derived from the Thermal Emission Imaging System (THEMIS): Thermal model and applications. *Journal of Geophysical Research*, *111*, E12004. https://doi.org/10.1029/2006JE002735

GUM (2008). Evaluation of measurement data Guide to the expression of uncertainty in measurement. Joint Committee for Guides in Metrology https://www.bipm.org/en/publications/guides/gum.html

Golombek, M., Grott, M., Kargl, G., Andrade, J., Marshall, J., Warner, N., et al. (2018). Geology and physical properties investigations by the InSight Lander. *Space Science Reviews*, *214*, 84. https://doi.org/10.1007/s11214-018-0512-7

Golombek, M., Kipp, D., Warner, N., Daubar, I. J., Fergason, R., Kirk, R. L., et al. (2017). Selection of the InSight Landing Site. *Space Science Reviews*, *211*(1-4), 5–95. https://doi.org/10.1007/s11214-016-0321-9

Golombek, M., Warner, N., Grant, J., Hauber, E., Ansan, V., Weitz, C., et al. (2020). Geology of the InSight landing site, Mars. *Nature Communications*, *11*, 1014. https://doi.org/10.1038/s41467-020-14679-1

Gómez-Elvira, J., Armiens, C., Castañer, L., Domínguez, M., Genzer, M., Gómez, F., et al. (2012). REMS: The environmental sensor suite for the Mars Science Laboratory Rover. *Space Science Reviews*, *170*, 583–640. https://doi.org/10.1007/s11214-012-9921-1

Grott, M. (2009). Thermal disturbances caused by Lander shadowing and the measurability of the Martian planetary heat flow. *Planetary and Space Science*, *57*, 71–77. https://doi.org/10.1016/j.pss.2008.11.005

Grott, M., Helbert, J., & Nadalini, R. (2007). Thermal structure of Martian soil and the measurability of the planetary heat flow. *Journal of Geophysical Research*, *112*, E09004. https://doi.org/10.1029/2007JE002905

Grott, M., Knollenberg, J., Borgs, B., Hänschke, F., Kessler, E., Helbert, J., et al. (2017). The MASCOT radiometer MARA for the Hayabusa 2 mission. *Space Science Reviews*, *208*, 413–431. https://doi.org/10.1007/s11214-016-0272-1

Grott, M., Knollenberg, J., Hamm, M., Ogawa, K., Jaumann, R., Otto, K. A., et al. (2019). Low thermal conductivity boulder with high porosity identified on C-type asteroid (162173) Ryugu. *Nature Astronomy*, 406. https://doi.org/10.1038/s41550-019-0832-x

Grott, M., Spohn, T., Knollenberg, J., Krause, C., Scharringhausen, M., Wippermann, T., et al. (2019). Calibration of the heat flow and physical properties package (HP^3) for the InSight Mars mission. *Earth and Space Science*, *6*, 2556–2574. https://doi.org/10.1029/2019EA000670

Hamm, M., Grott, M., Kührt, E., Pelivan, I., & Knollenberg, J. (2018). A method to derive surface thermophysical properties of asteroid (162173) Ryugu (1999JU3) from in-situ surface brightness temperature measurements. *Planetary and Space Science*, *159*, 1–10. https://doi.org/10.1016/j.pss.2018.03.017

Hiesinger, H., & Helbert, J. (2010). The Mercury Radiometer and Thermal Infrared Spectrometer (MERTIS) for the BepiColombo mission. *Planetary and Space Science*, *58*(1), 144–165. https://doi.org/10.1016/j.pss.2008.09.019

Kieffer, H. H. (2013). Thermal model for analysis of Mars infrared mapping. *Journal of Geophysical Research (Planets)*, *118*(3), 451–470. https://doi.org/10.1029/2012JE004164

Kopp, E., Mueller, N., Grott, M., Walter, I., Knollenberg, J., Hanschke, F., et al. (2016). HP3-RAD: A compact radiometer design with on-site calibration for in-situ exploration. In M. Strojnik (Ed.), *Infrared remote sensing and instrumentation XXIV* (Vol. 9973, pp. 99730T). San Diego, CA: SPIE. https://doi.org/10.1117/12.2236190

Maki, J. N., Golombek, M., Deen, R., Abarca, H., Sorice, C., Goodsall, T., et al. (2018). The color cameras on the InSight Lander. *Space Science Reviews*, *214*(6), 105. https://doi.org/10.1007/s11214-018-0536-z

Morgan, P., Grott, M., Knapmeyer-Endrun, B., Golombek, M., Delage, P., Lognonné, P., et al. (2018). A pre-landing assessment of regolith properties at the InSight landing site. *Space Science Reviews*, *214*(6), 104. https://doi.org/10.1007/s11214-018-0537-y

Morgan, P., Smrekar, S. E., Lorenz, R., Grott, M., Kroemer, O., & Müller, N. (2017). Potential effects of surface temperature variations and disturbances and thermal convection on the Mars InSight HP^3 heat-flow determination. *Space Science Reviews*, *211*, 277–313. https://doi.org/10.1007/s11214-017-0388-y

Mueller, N. (2019). Supplementary material for 'Calibration of the HP^3 radiometer on InSight' Retrieved from https:///dx.doi.org/10.6084/m9.figshare.c.4746179.v1

Pérez-Izquierdo, J., Sebastián, E., Martínez, G. M., Bravo, A., Ramos, M., & Rodríguez Manfredi, J. A. (2018). The Thermal Infrared Sensor (TIRS) of the Mars Environmental Dynamics Analyzer (MEDA) instrument onboard Mars 2020, a general description and performance analysis. *Measurement*, *122*, 432–442. https://doi.org/10.1016/j.measurement.2017.12.004

Planetary Data System (2019). Planetary Data System - InSight HP^3 RAD data archive urn:nasa:pds:insight_rad. https://pds-geosciences.wustl.edu/missions/insight/hp3rad.htm

Plesa, A.-C., Grott, M., Lemmon, M. T., Müller, N., Piqueux, S., Siegler, M. A., et al. (2016). Interannual perturbations of the Martian surface heat flow by atmospheric dust opacity variations. *Journal of Geophysical Research: Planets*, *121*, 2166–2175. https://doi.org/10.1002/2016JE005127

Plesa, A.-C., Grott, M., Tosi, N., Breuer, D., Spohn, T., & Wieczorek, M. A. (2016). How large are present-day heat flux variations across the surface of Mars? *Journal of Geophysical Research: Planets*, *121*, 2386–2403. https://doi.org/10.1002/2016JE005126

Plesa, A.-C., Padovan, S., Tosi, N., Breuer, D., Grott, M., Wieczorek, M. A., et al. (2018). The thermal state and interior structure of Mars. *Geophysical Research Letters*, *45*, 12,198–12,209. https://doi.org/10.1029/2018GL080728

Plesa, A.-C., Tosi, N., Grott, M., & Breuer, D. (2015). Thermal evolution and Urey ratio of Mars. *Journal of Geophysical Research (Planets)*, *120*(5), 995–1010. https://doi.org/10.1002/2014JE004748

Press, W., Teukolsky, S., Vetterling, W., & Flannery, B. (1992). *Numerical recipes in C* (2nd). Cambridge, UK: Cambridge University Press.

Preston-Thomas, H. (1990). The International Temperature Scale of 1990 (ITS-90). *Metrologia*, *27*(1), 3–10. https://doi.org/10.1088/0026-1394/27/1/002

Putzig, N. E., Mellon, M. T., Kretke, K. A., & Arvidson, R. E. (2005). Global thermal inertia and surface properties of Mars from the MGS mapping mission. *Icarus*, *173*(2), 325–341. https://doi.org/10.1016/j.icarus.2004.08.017

Ruff, S. W., Christensen, P. R., Blaney, D. L., Farrand, W. H., Johnson, J. R., Michalski, J. R., et al. (2006). The rocks of Gusev Crater as viewed by the Mini-TES instrument. *Journal of Geophysical Research: Planets*, *111*, E12S18. https://doi.org/10.1029/2006JE002747

Sapritsky, V. I., Khlevnoy, B. B., Khromchenko, V. B., Ogarev, S. A., Morozova, S. P., Lisiansky, B. E., et al. (2003). Blackbody sources for the range 100 K to 3500 K for precision measurements in radiometry and radiation thermometry. *AIP Conference Proceedings*, *684*(1), 619–624. https://doi.org/10.1063/1.1627196

Sebastián, E., Armiens, C., & Gómez-Elvira, J. (2010a). Pyrometer model based on sensor physical structure and thermal operation. *Applied Thermal Engineering*, *30*(16), 2403–2411. https://doi.org/10.1016/j.applthermaleng.2010.06.010

Sebastián, E., Armiens, C., & Gómez-Elvira, J. (2011). Infrared temperature measurement uncertainty for unchopped thermopile in presence of case thermal gradients. *Infrared Physics & Technology*, *54*(2), 75–83. https://doi.org/10.1016/j.infrared.2010.12.038

Sebastián, E., Armiens, C., Gómez-Elvira, J., Zorzano, M. P., Martinez-Frias, J., Esteban, B., & Ramos, M. (2010b). The Rover environmental monitoring station Ground Temperature Sensor: A pyrometer for measuring ground temperature on Mars. *Sensors*, *10*(10), 9211–9231. https://doi.org/10.3390/s101009211

Siegler, M. A., Smrekar, S. E., Grott, M., Piqueux, S., Mueller, N., Williams, J.-P., et al. (2017). The InSight Mars Lander and its effect on the subsurface thermal environment. *Space Science Reviews*, *211*, 259–275. https://doi.org/10.1007/s11214-017-0331-2

Smrekar, S. E., Lognonné, P., Spohn, T., Banerdt, W. B., Breuer, D., Christensen, U., et al. (2019). Pre-mission InSights on the interior of Mars. *Space Science Reviews*, *215*(1), 3. https://doi.org/10.1007/s11214-018-0563-9

Spiga, A., Banfield, D., Teanby, N. A., Forget, F., Lucas, A., Kenda, B., et al. (2018). Atmospheric science with InSight. *Space Science Reviews*, *214*(7), 109. https://doi.org/10.1007/s11214-018-0543-0

Spohn, T., Grott, M., Smrekar, S. E., Knollenberg, J., Hudson, T. L., Krause, C., et al. (2018). The heat flow and physical properties package (HP^3) for the InSight mission. *Space Science Reviews*, *214*, 96. https://doi.org/10.1007/s11214-018-0531-4

Spohn, T., Knollenberg, J., Ball, A. J., Banaszkiewicz, M., Benkhoff, J., Grott, M., et al. (2015). Thermal and mechanical properties of the near-surface layers of comet 67P/Churyumov-Gerasimenko. *Science*, *349*(2), aab0464. https://doi.org/10.1126/science.aab0464

Spohn, T., Seiferlin, K., Hagermann, A., Knollenberg, J., Ball, A. J., Banaszkiewicz, M., et al. (2007). Mupus—A thermal and mechanical properties probe for the Rosetta Lander Philae. *Space Science Reviews*, *128*, 339–362. https://doi.org/10.1007/s11214-006-9081-2

Vasavada, A. R., Piqueux, S., Lewis, K. W., Lemmon, M. T., & Smith, M. D. (2017). Thermophysical properties along Curiosity's traverse in Gale crater, Mars, derived from the REMS Ground Temperature Sensor. *Icarus*, *284*, 372–386. https://doi.org/10.1016/j.icarus.2016.11.035

Walter, I., Hirsch, H., Jahn, H., Knollenberg, J., & Venus, H. (2006). MERTIS: A highly integrated IR imaging spectrometer. In M. Strojnik (Ed.), *Infrared spaceborne remote sensing XIV* (pp. 249–259). San Diego, CA: SPIE. https://doi.org/10.1117/12.679481